NEXTGEN AERONAUTICS
2780 Skypark Drive, Suite 400
Torrance, CA 90505

CONTRACT NO. NNX15AW45G

VERSATILE EXPERIMENTAL AUTONOMY RESEARCH AIRCRAFT TECHNOLOGY (VEARAT)

SUMMARY OF RESEARCH, FINAL

Period of Performance:
15 October 2015 – 31 January 2017

NextGen TPOC:
Dr. Shiv Joshi
(t) 310.626.8360; (f) 310.891.2825
(e) sjoshi@nextgenaero.com

Co-Investigators:
Dr. R. Kapania, Virginia Tech
Dr. G. Chowdhary, University of Illinois Urbana-Champaign

Issued by:
NASA/Shared Services Center (NSSC)
Building 1111, Jerry Hlass Road
Stennis Space Center MS 39529-0001

TABLE OF CONTENTS

1 INTRODUCTION 2
2 DESIGN MODIFICATIONS 4
2.1 Propulsion System Improvements 4
2.2 Airframe Optimization 7
2.2.1 Optimization of BASSET Wing 7
2.2.2 Development of NASTRAN Finite Element Model 8
2.2.3 Optimization of VEARAT 9
2.2.4 Development of NASTRAN Finite Element Model 9
2.3 Manufacturing of VEARAT 10
2.4 GNC Approach 11
2.4.1 Hardware Design 11
2.4.2 Software Design 14
2.4.3 GNC Test Aircraft 15
2.5 GNC and Payload Hardware Integration 16
3 RESULTS AND DISCUSSION 18
3.1 Propulsion System Aerodynamic Impact Analysis 18
3.2 Structual Optimization 20
3.2.1 Applied Load Distribution for BASSET NASTRAN Wing-box Model 20
3.2.2 BASSET Wing Optimization Results 22
3.2.3 Applied Loads on VEARAT 25
3.2.4 VEARAT Wing Optimization Results 28
3.2.5 FEM Optimization Conclusions 30
3.2.6 CAD Modeling of FEM Optimized Wing Structure 30
3.2.7 VEARAT Mass Savings 32
3.3 GNC Flight Test Results 33
3.3.1 Stable Flights 33
3.3.2 Autonomous Waypoint Guidance 35
3.3.3 Autonomous Landing 39
4 CONCLUSIONS AND RECOMMENDATIONS 45
5 REFERENCES 46

LIST OF FIGURES

Figure **Page**

1: Point of Departure NextGen designed BASSET UAV 3
2: HKS 700E Engine..... 5
3: 64" 3 Bladed Pitch Adjustable Prop – Comparison of Disc Area to Baseline 6
4: Comparison of VEARAT vs. BASSET Configurations – Wing Span and Tail Boom Width..... 6
5: BASSET UAV Wing Geometry 7
6: CAD Model of BASSET Wing-box 8
7: BASSET Finite Element Mesh (a) Without Skin, (b) With Skin 9
8: CAD Model of VEARAT 9
9: FEM of VEARAT..... 10
10: Boundary Conditions of VEARAT..... 10
11: Original BASSET Molds 11
12: Block Diagram showing Modules of the Autopilot..... 12
13: BeagleBone Black..... 12
14: VectorNav VN-200 Rugged GPS/INS 13
15: jDrones jD RF900 Plus 13
16: Systems Integration Board..... 14
17: Fail-Safe Servo Driver 14
18: Block Diagram of Thread Design..... 15
19: SkyHunter Airframe and Specifications 16
20: BASSET Payload Bay - Example Integration of an Experimental Radio Payload 16
21: BASSET Flight Control Box - Reconfigured for Stabilis System..... 17
22: Conceptual Integration of K-band DAA Radar 18
23: Conceptual Integration of Complete Stabilis DAA System 18
24: L/D Performance Comparison – BASSET vs. VEARAT 19
25: VEARAT - 55 KEAS - AOA = 2.5 - Streamline and Pressure Contour Plots 19
26: Pitching Moment vs. Lift Coefficient – BASSET vs. VEARAT 20
27: CFD Pressure Distribution..... 21
28: Pressure Distribution at Test Section..... 21
29: Location of Center of Pressure along the Span..... 21
30: Applied Forces 22
31: BASSET Optimization Results for 3.35 g Load Case 23
32: Stress Distribution: BASSET Optimization for 3.35 g Load Case..... 23
33: Constraint Activity - BASSET Optimization for 3.35 g Load Case..... 24
34: BASSET Optimized Thickness Distribution, 3.35 g Load Case 24
35: Comparison of BASSET Optimized Results, 3.35 g and 5 g 25
36: CFD Pressure Distribution on Upper and Lower Skins..... 26
37: Adjusted Pressure Distribution on the Upper Skin..... 26
38: Adjusted Pressure Distribution on the Lower Skin 27
39: Location of Center of Pressure along the Span..... 27

LIST OF FIGURES (CONT)

Figure **Page**

40: Applied Loads on VEARAT FEM 28
41: Stress Distribution - Load 2, Load Subcase 1 28
42: Stress Distribution - Load 2, Load Subcase 2 29
43: VEARAT Structural Optimization Results 29
44: VEARAT Load Case 2 Optimized Member Thickness (a) Spar Cap and (b) Spar Web 30
45: Detail Designed Optimized VEARAT Wing Structure 31
46: Location of Mass Distribution Points 32
47: Stable Flight, Tracking Performance of Aircraft to Commanded Roll 34
48: Stable Flight, Tracking Performance of the Aircraft to Commanded Roll: Post Flight Filtered Data 34
49: Stable Flight, Tracking Performance of the Aircraft to Commanded Pitch: Post Flight Filtered Data 35
50: Autonomous Waypoint Guidance: STABILIS Autopilot on Skyhunter Flight Test 36
51: Commanded Roll Attitude Tracking for Autonomous Waypoint Guidance 36
52: Commanded Pitch Attitude Tracking for Autonomous Waypoint Guidance 37
53: Autonomous Waypoint Guidance - STABILIS Autopilot on SkyHunter, HIL Test (No Cross Wind) 37
54: Commanded Roll Attitude Tracking for Autonomous Waypoint Guidance - HIL Test (No Cross Wind) 38
55: Commanded Pitch Attitude Tracking for Autonomous Waypoint Guidance - HIL Test (No Cross Wind) 38
56: Stall Recovery Maneuver - UAV Pitch Attitude demonstrating Stall, Loss of Lift and Altitude, and Recovery Phase 39
57: Roll Attitude of Vehicle while Stall Recovery Maneuver 39
58: Cross Wind effects on the Landing of Aircraft 40
59: Ground Effect on Landing of Aircraft 40
60: Pitch and Altitude Control to achieve Autonomous Landing 41
61: Landing Trajectory: Ground Track vs Altitude 41
62: UAV Achieved Attitude Angles Time Plot while Performing Landing 42
63: Landing Trajectory: Initial Condition: Course Angle 80 degrees to North, Landing Orientation: 0deg North 42
64: Aircraft Velocities and Attitude Angles in Body Frame, While Executing the Autonomous Landing 43
65: Aircraft Time Plot for Position in Landing Approach and Landing Phase 43
66: Autonomous Landing in SIL Simulations in Xplane and MATLAB 44
67: SIL Landing Results: UAV Landing Trajectory, Cross Track (North and East) and Altitude Time Plot 44
68: SIL Landing Simulations: UAV Attitude Angle and Body Rates Plots 45

LIST OF TABLES

Table **Page**

1: Evaluated Engine Options 5
2: BASSET vs. VEARAT - Aircraft Reference Parameters 7
3: Comparison of Member Weight 25
4: Mass Distribution of Detail Designed Optimized VEARAT Wing Structure 31
5: Detail Design Wing Structural Weight Savings after Optimization 32
6: Projected VEARAT Structural Weight Savings 32
7: VEARAT Vehicle Endurance Enhancements 33

ACKNOWLEDGEMENTS

The reported work is performed by NextGen Aeronautics in cooperation with the University of Illinois Urbana-Champaign (UIUC) and Virginia Polytechnic Institute and State University (Virginia Tech).

- NextGen Aeronautics: Shiv Joshi, Matt Scott, Rob Bortolin, John Flanagan, and Robbie Snyder
- UIUC: Professor Girish Chowdhary and Girish Joshi
- Virginia Tech: Professor Rakesh Kapania, Professor Joe Schetz, and Wrik Mallick

UIUC and Virginia Tech contributed to autopilot and structural optimization research, respectively.

Dr. Koushik Datta provided guidance to the team as a NASA program manager. The NextGen team is thankful for his leadership and breadth of technical expertise which was invaluable in successfully executing the program.

The NextGen team is also thankful to Dr. David Voracek and Dr. John Ryan from NASA Armstrong Flight Research Center for suggesting desired capabilities of an experimental autonomy research vehicle.

Versatile Experimental Autonomy Research Aircraft Technology (VEARAT)

PI: S. Joshi, NextGen Aeronautics
Co-Investigators: R. Kapania, Virginia Tech;
G. Chowdhary, University of Illinois Urbana-Champaign

ABSTRACT

The Versatile Experimental Autonomy Research Aircraft Technology (VEARAT) program is envisioned to develop system architectures and technologies that would enable VEARAT UAV to easily integrate, verify, and validate rapidly evolving hardware and software subsystems for autonomous flight. Our approach to materialize program goals is to initiate development based on an existing technology demonstrator to reduce cost of development and prototype construction. It is a UAV designed, fabricated and tested by NextGen Aeronautics. The VEARAT UAV will allow nontraditional technologies such as open-source software and consumer electronics products from autonomy experimentalists to be tested with minimum risk by the switchable robust base system taking over control from nontraditional technologies being tested when it demonstrates spurious behavior. The VEARAT program focused on several design improvements that have potential to transform the existing flight tested UAV into a complete system for autonomy research. Design improvements are made to increase endurance to more than six hours to provide experimental autonomy research utility at reasonable cost. Subsystems include BLOS communication, detect and avoid sensor systems and hazardous weather avoidance. The autopilot is capable of autonomous takeoff, flight, and landing.

The VEARAT UAV design includes efficient engine, increased propeller diameter and structural weight optimization. Autopilot with modularized subsystems with "Plug-and-Play" logic for switching subsystems with units supplied by experimenter, and multiple communication channels. GNC software is multi-threaded and includes deterministic and non-deterministic hierarchical and adaptive baseline algorithms. Software by experimenter can be uploaded and modified in real-time during HIL ground and flight testing while aircraft is autonomously flown by baseline autopilot. The proposed autopilot system also allows SIL inflight forward predictions.

NextGen Aeronautics, working cooperatively with NASA, can provide versatile experimental autonomy research UAV(s) available to the research community at a fraction of the cost needed for autonomy hardware/software verification and validation.

1 INTRODUCTION

The National Research Council's report [1] described the contributions that advances in autonomy could make towards civil aviation, identified key barriers to implementation, and provided a national research agenda for enabling the introduction of autonomy into civil aviation. This report identified the following substantial barriers to the increased use of autonomy in civil aviation systems and aircraft:

- Technology Barriers
  - Communications and data acquisition
  - Cyberphysical security
  - Decision making by adaptive/nondeterministic systems
  - Diversity of aircraft
  - Human–machine integration
  - Sensing, perception, and cognition
  - System complexity and resilience
  - Verification and validation
- Regulation and Certification Barriers
  - Airspace access for unmanned aircraft
  - Certification process
  - Equivalent level of safety
  - Trust in adaptive/nondeterministic IA systems
- Additional Barriers
  - Legal issues
  - Social issues

The Versatile Experimental Autonomy Research Aircraft Technology (VEARAT) program was envisioned under the NASA LEARN2 project for developing system architectures and technologies that would enable experimental autonomous unmanned aircraft to easily integrate, verify and validate rapidly evolving hardware and software subsystems. Our approach to materialize NASA LEARN2 goals is to initiate development based on an appropriate technology demonstrator. An unmanned aerial vehicle (UAV) designed, fabricated and tested by NextGen named BASSET (Big Antenna Small Structure Enhanced Tactical) UAV was developed under an Air Force program (Contract No. FA8650-08-C-3845). NextGen's intent is to allow nontraditional technologies such as open-source software and consumer electronics products from an autonomy experimentalist to be tested with minimum risk by the robust base system taking over control from adaptive non-deterministic third party systems when needed.

The goal of the VEARAT program is to design a versatile autonomy research aircraft. NextGen proposed to increase autonomous operations time of BASSET without real-time human cognizance and control to allow long duration autonomy experiments. The technical objectives to attain this goal are:

- Design enhancement of BASSET UAV to allow interchangeable sensors and communication hardware
- Introduce capability to vary aircraft performance and controllability for different experiments
- Plug-and-play payloads capability
- Easy software uploading and hardware-in-loop (HIL) ground testing
- Deterministic and non-deterministic hierarchical and adaptive guidance, navigation, and control (GNC) baseline hardware and algorithms
- Flight termination system (FTS)
- Seamless autonomous/human control handover
- Design a resilient system that is capable of adapting to platform and mission changes.

Figure 1 shows the BASSET UAV developed for communication subsystems testing by NextGen under Air Force funding during 2008-2013.

Figure 1: Point of Departure NextGen designed BASSET UAV

The designed and fabricated BASSET UAV has available space for replaceable subsystems and it was designed with modular major structural parts that are stored in a standard C-130 pallet. It can be assembled from the box to airborne in 30 minutes. It has an integrated FTS and an autonomous/human switchable GNC system. The NextGen team proposed to optimize the BASSET UAV design to maximize autonomy research versatility and introduce plug-and-play simplicity for users. The key accomplishments of BASSET UAV development included the following:

- Within $3.8 M, the team developed the BASSET concept, completed design, fabrication, and testing of the BASSET aircraft, flight tested the NGC ISR/SIGINT payload, and developed (in-house) and flight tested a direction finding demonstration payload.
- The flight testing established basic flight characteristics, performance, and operations, demonstrated antenna performance and validated direction finding /geolocation and other RF capabilities.

- The BASSET aircraft stands as a capable, portable, platform with significant payload carrying capability.

The VEARAT program focused on several design improvements that have potential to transform the BASSET UAV into a complete system for autonomy research:

1. INCREASED ENDURANCE: An endurance of 6+ hrs with a payload capacity of between 50 to 100 lbs has been achieved to provide experimental autonomy research utility at reasonable cost.
2. BEYOND LINE OF SIGHT (BLOS) COMMUNICATIONS: This can be accomplished with the proposed GNC system, leveraging cellular networks or radios in the VHF band (300 Mhz)
3. FULLY AUTONOMOUS OPERATIONS: The current system is capable of way-point navigation but requires an operator for takeoffs and landings; these can be automated, completely removing the pilot from the loop.
4. COOPERATIVE AND NONCOOPERATIVE VEHICLE AVOIDANCE: This will require additional subsystems to be integrated in the UAV. More specifically, we will integrate an ADS-B transceiver and K-band radar.

Section 2 describes methods and procedures used to produce a preliminary design of VEARAT vehicle. Results are discussed in Section 3, as well as flight simulations and surrogate vehicle flight testing of the autopilot. Conclusions and recommendations are presented in Section 4.

2 DESIGN MODIFICATIONS

Our technical approach to complete the design of the VEARAT UAV is to start with the BASSET UAV that has been flight tested. We will improve the design for versatility and performance using multidisciplinary optimization as well as include an autopilot with capability to take inputs from user specified sensors.

2.1 Propulsion System Improvements

The propulsion system of BASSET was identified for modification to increase endurance of the VEARAT aircraft. As with many aircraft programs, the BASSET development program was subjected to feature creep and the result was a suboptimal propulsion system. While take-off and climb performance was adequate, fuel consumption of the baseline engine exceeded manufacturer's specifications by a factor of two. Furthermore, test stand versus installed thrust testing indicated that prop efficiency suffered because of being occluded by the fuselage. Both of these performance deficiencies have been addressed under the LEARN2 program.

The baseline BASSET engine was a high-end large scale RC hobbyist engine. As such, it lacked quality control and end user support that would be typical of any engine used by manned aircraft. Power requirements (60 Hp) and weight constraints (200 lbs including 6 hours of fuel) for VEARAT are well aligned with ultralight aircraft engines, accordingly the surveyed trade space was a range of ultralight aircraft engines. Many of these engines had long records of performance and maintenance data, and active user communities supporting their continued use. Table 1 details the range of engines researched, with the BASSET baseline appearing at the top, and the final selection of the HKS 700E at the bottom.

Table 1: Evaluated Engine Options

Engine	HP	Cost	Fuel	Cooling	Dry Weight	Cruise SFC [lb/hp/hr]	Mission Weight [lb]
3W-684 iB4 – BASSET BL	**40**	**$7,810**	**100 LL**	**Air**	**37**	**1.35**	**361**
CRE MZ202	60	$6,000	Super 95 RON / MON 85	Forced Fan	87	0.58	199
Hirth 3203	65	$5,150	unleaded 93 octane auto fuel	Free air or fan	79	0.43	209
Hirth 3502	60	$5,480	Assumed 93 octane @50:1	liquid	79 [1]	0.43	198 [2]
Rotron RT600LCR	58	$34,000	Assumed AvGas[3]	liquid	66	0.61	225 [2]
Simonini Victor 1 Super	54	$6,000	Assumed MoGas[3]	Air[4]	68	0.22	123
UAV Engines Ltd Ar 682	75	$23,150	100LL or min 92 RON moGas	Water	108	0.54	257 [2]
HKS 700E - Selected	**60**	**$11,500**	**92 Octane**	**Air**	**121**	**0.32**	**210**

[1] Radiator not included in weight numbers; [2] Liquid coolant not included in weight; [3] No fuel type provided, assumption based on similar engine in manufacturers lineup; [4] Liquid cooling option available; 2.5 lb + coolant

The HKS 700E engine was selected for its reliability and efficient 4-stroke operation. Its selection allowed for the use of a much larger diameter propeller (64" vs. 36"), offering a 275% increase in prop disc area. A number of propeller manufacturers produce suitable props with adjustable blade pitch in this diameter range. This will allow the prop configuration to be tailored to the mission requirements of any flight plan. Specific fuel consumption was improved by a factor of three, and the integral electronic auto-start will ensure safer operations. The standard alternator outputs 210 watts, which will be adequate for onboard systems with ample battery back up. The HKS 700E engine is pictured in Figure 2, while the propeller selection and change in prop disk area is highlighted in Figure 3.

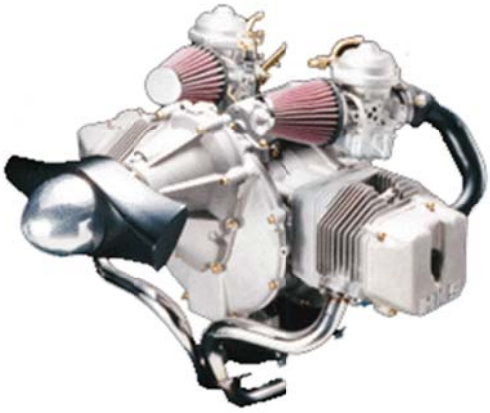

Figure 2: HKS 700E Engine

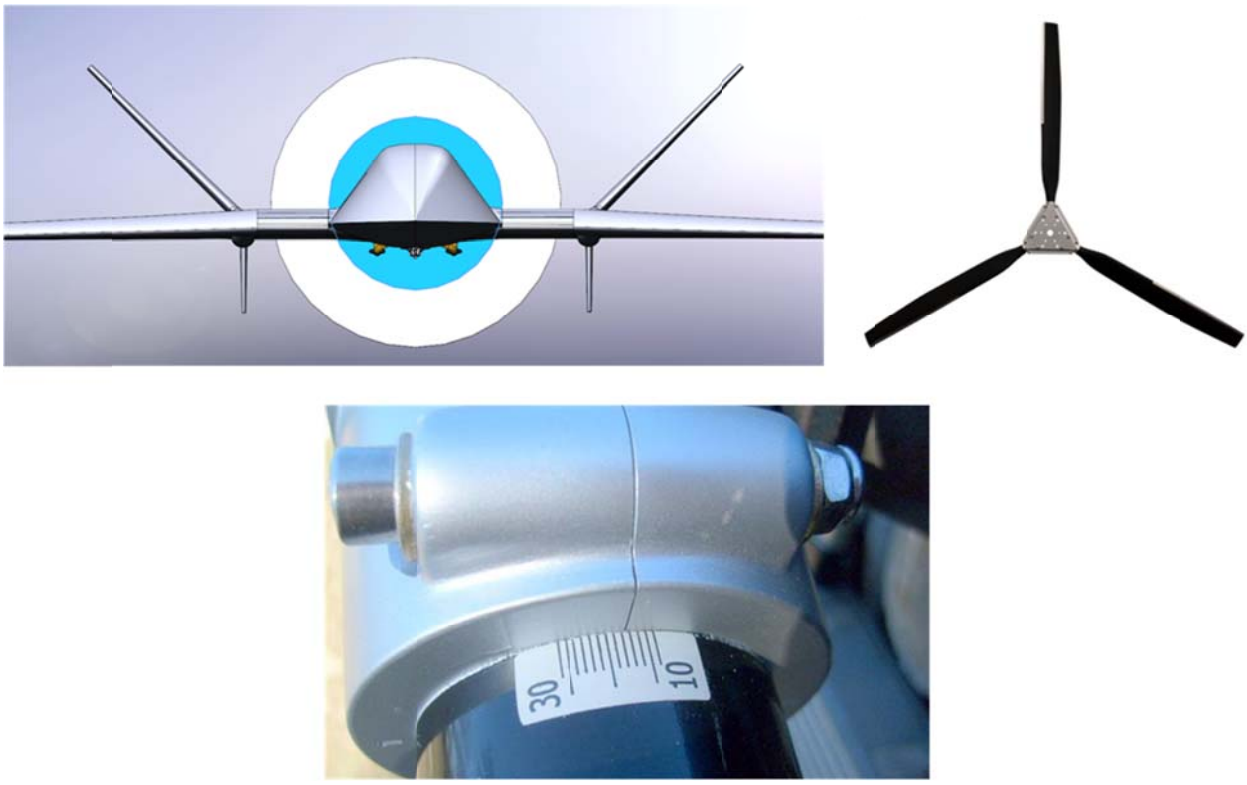

Figure 3: 64" 3 Bladed Pitch Adjustable Prop – Comparison of Disc Area to Baseline

Integration of the HKS 700 engine and large diameter prop required an adjustment of the vehicle planform. The baseline tail boom spacing of 37" was increased to 65" to accommodate the 64" diameter prop. To minimize the impact on aircraft performance and utilize existing tooling to the maximum extent possible, the overall wing and tail span was increased proportionally. Modularity of the primary wing panel was retained, as the interface was shifted outboard with the baseline wing panel. Figure 4 shows the difference in wing span and tail boom width between the BASSET and VEARAT configurations, and Table 2 provides a quantitative comparison of common aircraft parameters.

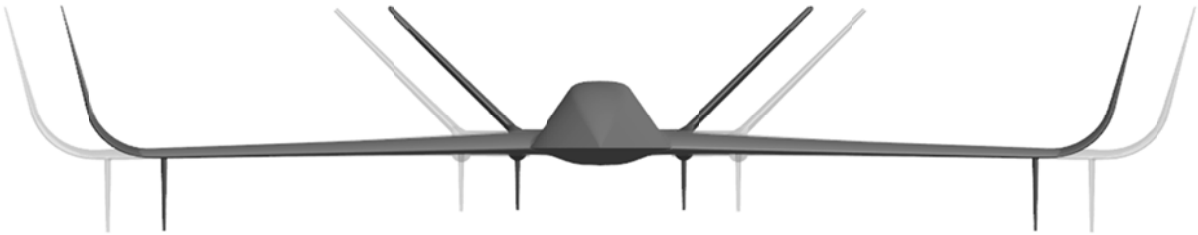

Figure 4: Comparison of VEARAT vs. BASSET Configurations – Wing Span and Tail Boom Width

Table 2: BASSET vs. VEARAT - Aircraft Reference Parameters

Parameter	BASSET	VEARAT	VEARAT / BASSET
Wing planform area [ft^2]	50.5	58.8	16%
Wing span [ft]	22.7	25	10%
Wing MAC [ft]	2.68	2.82	5%
Wing AR	10.2	10.6	4%
H-tail planform area [ft^2]	12.8	16.8	31%
H-tail Xac [ft]	15.7	16.1	3%
H-tail volume coefficient	0.74	0.84	14%

2.2 Airframe Optimization

First, the original BASSET vehicle wing is optimized to realize weight saving. Structural optimization of the wing-box was performed using MSC NASTRAN's design optimization tool. Then, the wing-box of the modified version of BASSET, VEARAT, is also optimized using the MSC NASTRAN design optimization tool.

2.2.1 Optimization of BASSET Wing

The BASSET wing geometry is defined by an Eppler 396 airfoil section, which is a highly cambered airfoil of modest thickness designed for high lift applications. The root chord is just over 3.5' and the angle of incidence at this location is a positive 3°. The wing has a leading edge taper with a total taper ratio of 0.42, and therefore the tip chord is about 1.5'. Along the length of the span, the inboard incidence of positive 3° washes out to a value of 0° at the tip. The wing has a planform area of 45.74 ft^2 and a span of 18', which amounts to an aspect ratio of 7.08. The mean aerodynamic chord is 2.68', with the wing aerodynamic center Xac = 94.31" aft of the nose. Figure 5 summarizes the wing geometry parameters and shows the reference geometry used to obtain these values.

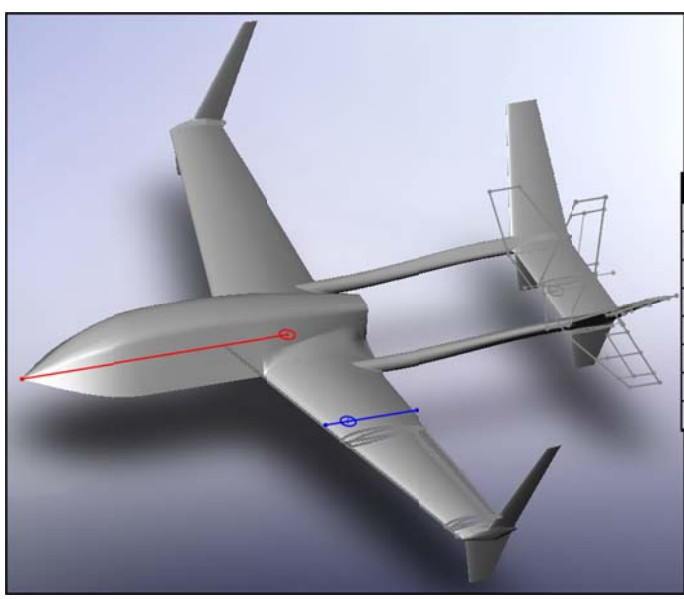

BASSET UAV Wing Parameters	
Wing Area [ft^2]	45.74
Span [ft]	18.0
Wing Xac [in]	94.31
Root Chord [ft]	3.58
Taper Ratio	0.42
MAC [ft]	2.68
Aspect Ratio	7.08
Airfoil Definition	Eppler 396

Figure 5: BASSET UAV Wing Geometry

Load cases for sizing the aircraft were obtained using ANSYS CFX fluid simulations of the BASSET configuration at a design point of 55 knots and 2000 ft. mean sea level (~1000 ft. above ground level at McMillan Field). For this design point, an earlier version of the BASSET was capable of generating 435 lbs. of lift at an angle of attack (AOA) of 2.9°. Of the 435 lbs., 86% the wing weight or 375 lbs. is the contribution from the wing and winglets. For one wing and winglet pair, this equates to 187.8 lbs. of lift and a root bending moment of 12,094 in-lbs. (at vehicle centerline). At 5g limit load, these figures increase to 939 lbs. of lift and 60,471 in-lbs. of moment. These loads were supplemented with a safety factor of 1.25. The structure was then sized using 3D finite element analysis (FEA) in ANSYS.

As the vehicle weight increased from 440 lbs. to 650 lbs., a new computational fluid dynamics (CFD) simulation was performed to obtain the trim loads. The new loads now set a limit load of 3.35g to match the overall lift from the previous load case so that the wing can sustain the aerodynamics loads. The optimization study will be performed for the updated vehicle weight and aerodynamics loads.

2.2.2 Development of NASTRAN Finite Element Model

A finite element model (FEM) was developed in NASTRAN based on the CAD model of the wing as shown in Figure 6.

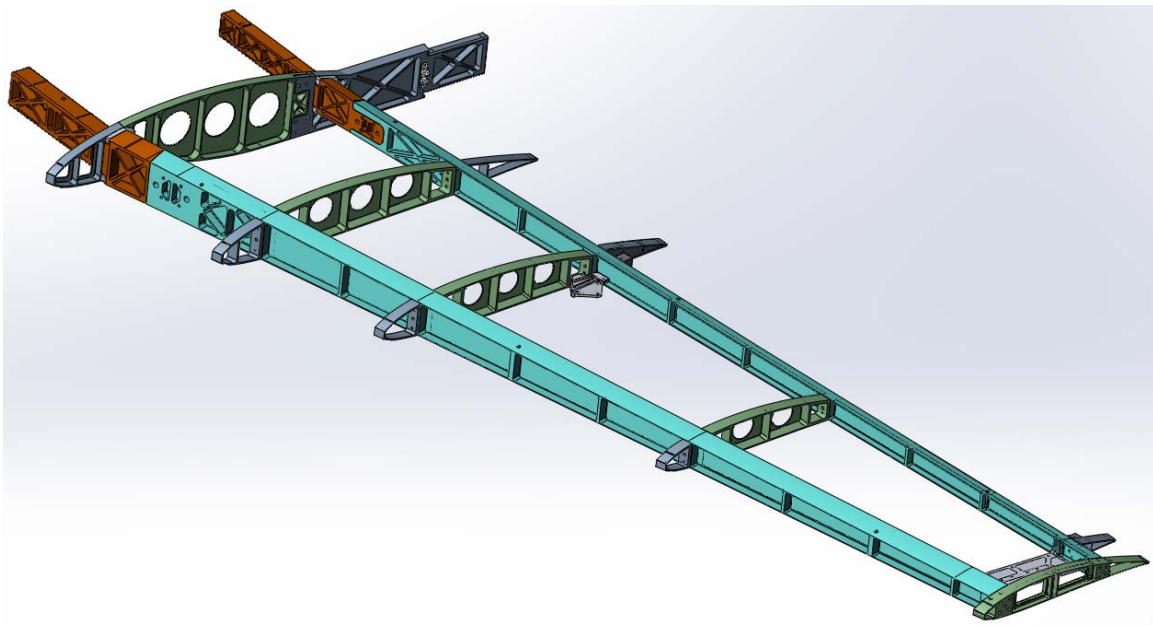

Figure 6: CAD Model of BASSET Wing-box

Certain assumptions were used to develop the FEM. First, only that section of the rib was modeled which lied within the wing-box. Secondly, the whole wing-box was modeled using two-dimensional plate elements (PSHELL) in NASTRAN. Thus, the three-dimensional features of the root spar (as shown in Figure 6) could not be captured. Also, the wing was modeled using a combination of 4-noded quadrilateral (CQUAD4) and 3-noded (CTRIA3) triangular elements. As such, the exact curvilinear shape of the ribs and the holes could not be captured. The skin was added to the structure model unlike the CAD model. Also the same Al 7075-T6 as used for the rest of the vehicle was used for the skin instead of composites. The wing outer mold line (OML), twist and dihedral were captured accurately. The finite element mesh is shown in Figure 7. From

Figure 7(a), one can see that polygonal holes with equal area to that of the circular holes were used in the FEM.

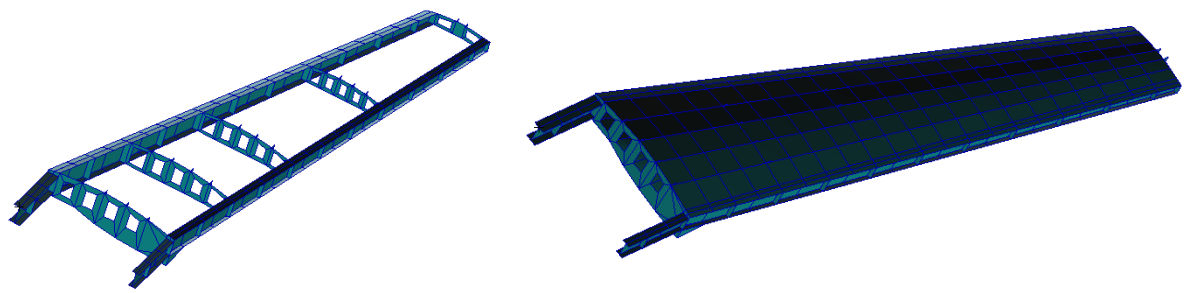

(a) (b)

Figure 7: BASSET Finite Element Mesh (a) Without Skin, (b) With Skin

The skin thickness distribution, the spar cap, and spar web thickness distributions, were considered as the design variables in the optimization study. The skin stiffeners, ribs and rib stiffeners were modeled using the baseline thickness. The limitation of a minimum thickness of 0.04" for the spar caps and 0.03" for other members were maintained. The von Mises stresses on the upper and lower surface of each element were considered as the design constraints.

2.2.3 Optimization of VEARAT

The VEARAT is a modified version of the BASSET configuration with the tail booms shifted 14" outboard on each side, the overall wing span increased from 22.7’ to 25’ and the center-body extended outboard of the tail booms. While there is no baseline sizing of the VEARAT available, the weight reduction of the BASSET structural optimization study motivated an analogous design optimization study of the VEARAT configuration.

2.2.4 Development of NASTRAN Finite Element Model

The VEARAT NASTRAN FEM was developed in an analogous way to the BASSET. The CAD model of the half-span VEARAT is shown in Figure 8. It shows that the spars in the VEARAT do not end in a plug receptacle in the fuselage but is instead carried through. Thus, the wing is a continuous member through the fuselage. The present study will focus on the structural aspects of the half-span only since we are looking at symmetric load cases.

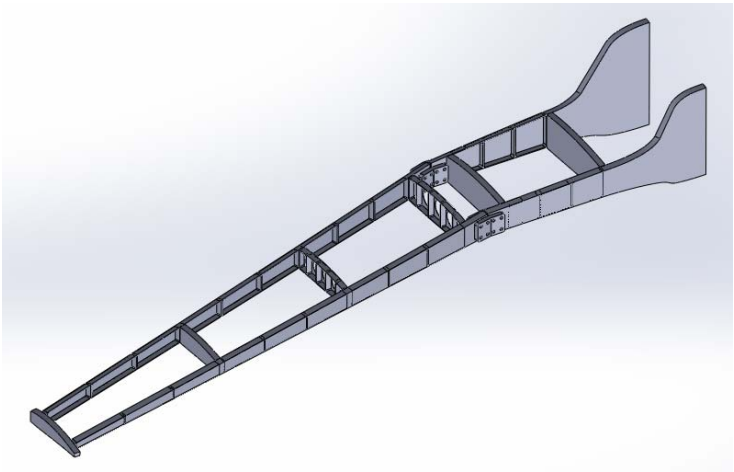

Figure 8: CAD Model of VEARAT

All the wing-box members were modeled using CQAUD4 or CTRIA3 PSHELLs available in NASTRAN. Thus, curvilinear nature of the ribs and the holes could only be approximated as rectangular sections. The finite element mesh of VEARAT configurations with and without the skins is shown in Figure 9. Fixed boundary condition was applied to all the nodes which lied inside the fuselage and was connected to the bulkhead. The boundary conditions are shown in Figure 10.

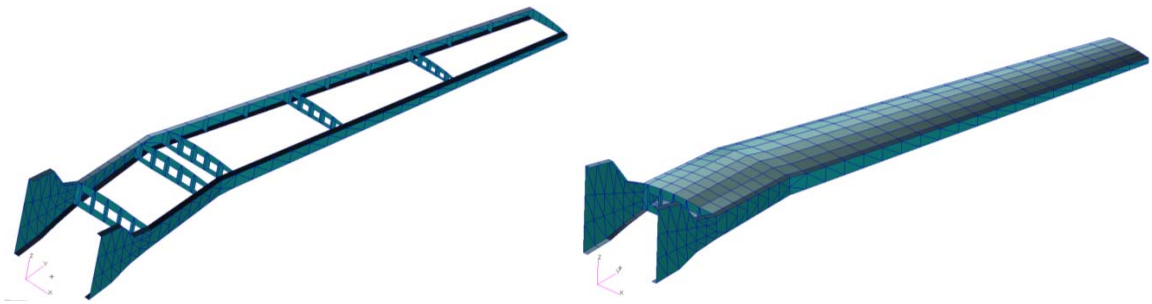

Figure 9: FEM of VEARAT

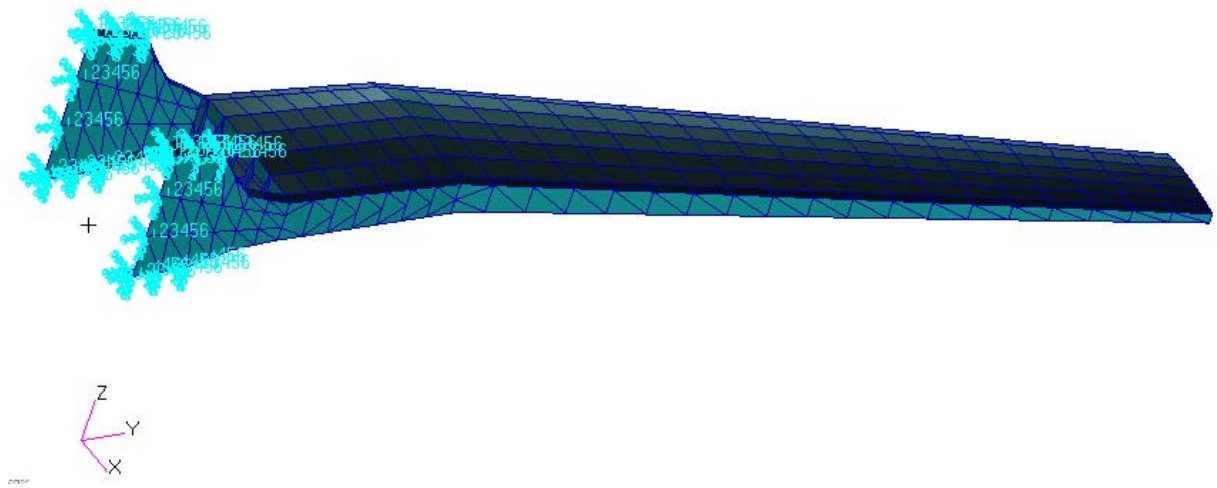

Figure 10: Boundary Conditions of VEARAT

2.3 Manufacturing of VEARAT

Because the BASSET flight vehicle has already been manufactured and flight-tested the tooling and molds for the aircraft currently exist. Special care was taken during the development of the VEARAT design to ensure that minimal impact is made to preexisting tooling to minimize non-recurrent manufacturing costs. The main areas of change with regard to aircraft OML are the wing and horizontal tail areas. The extensions to both of these areas were done to accommodate the larger propeller chosen for VEARAT. The major impact to manufacturing these areas is in the molds for the carbon fiber skins. Specifically the molds will not have to be completely remanufactured, but instead the design allows for additions to the molds to build up the longer wing and horizontal tail sections. This will dramatically reduce the cost associated with retooling by not creating all new molds. The molds can be seen in Figure 11.

Figure 11: Original BASSET Molds

2.4 GNC Approach

2.4.1 Hardware Design

The design and development of the autopilot uses a new approach by modularizing the subsystems in the autopilot. Using the process, the system can be prevented by becoming obsolete with the advancements in technology. Being modular helps in the development of the autopilot to be mission specific as well. Furthermore, any faulty subsystems can be easily replaced individually without affecting the whole system.

The components that were chosen to feature modularity are:

- Flight Control Computer
- Inertial Navigation System (INS)
- Wireless Ground Control Communications

When selecting the components for aerospace design, the form factor, the weight and the power consumption of all the components play a major role. Figure 12 shows the various components and their communication protocols.

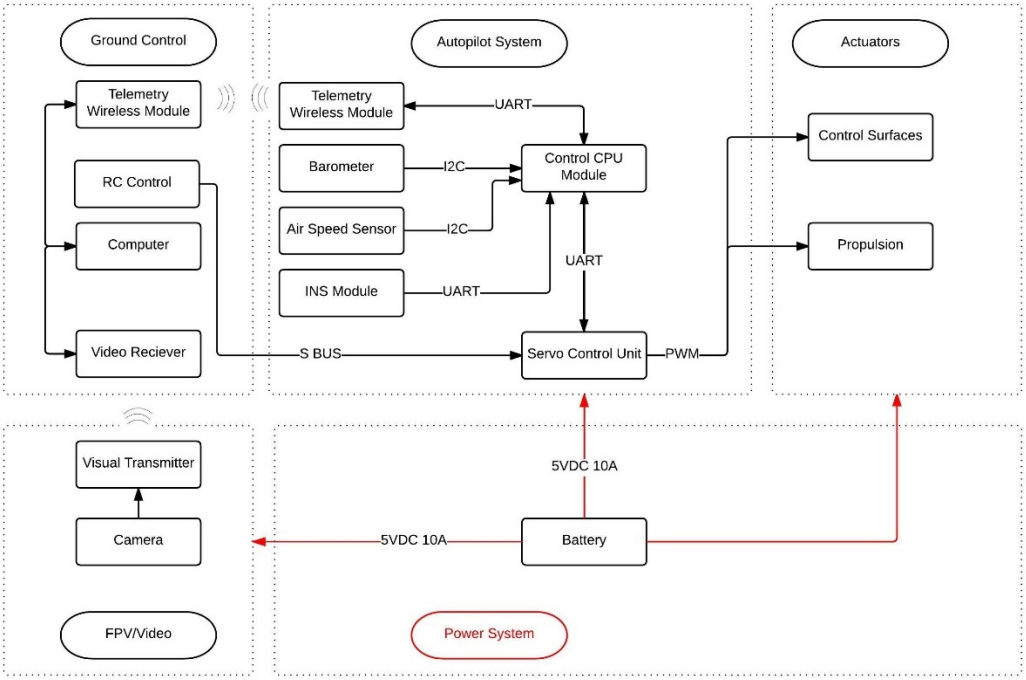

Figure 12: Block Diagram showing Modules of the Autopilot

Modular Components

Flight Control Computer: The flight control computer handles all the operations such as interacting with all the components on-board the aircraft, as well as communicating with the ground control station. Its primary functions include:

- Analyzing the data received from the onboard sensors.
- Executing the flight controls
- Communicating with the Ground Control Station
- Logging flight data for post-flight analysis

Figure 13: BeagleBone Black

Special attention was needed with considering the size, weight, power consumption and I/O ports configuration. The suitable choice was the BeagleBone Black, an embedded computer board (Figure 13).

The BeagleBone Black features:

- Sitara AM3358 1Ghz ARM \textregistered - A8 32-Bit Processor
- 512 MB DDR3 RAM
- 4GB 8-bit eMMC on-board flash storage
- 2x PRU 32-bit microcontrollers

Usually, the autopilots are designed and developed around the selection of the central computer. But in our approach to the design of the autopilot, the flight control computer is also modular

since the selection of the subcomponents can be easily adapted to fit other similar linux-based embedded computers by simply modifying the routing and connections of the Systems Integration Board (SIB). However, the makers of BeagleBone Black have not changed the form factor for 4 generations of development. Therefore, it is safe to assume, BeagleBone Black can be easily replaced with an upgraded version from BeagleBone in the future with no modifications.

Navigation Sensors: Navigation sensors provide reliable measurement for the flight status of the flying vehicle. Many commercial navigation sensors are available on the market. All of them vary in the material, manufacturing technology, measuring range, size, weight, estimation algorithm, positional accuracies. Based on the working principle, a navigation solution falls into one of these categories:

- INS
- INS/GPS (INS calibrated by GPS)
- GPS-aided AHRS

It is a common practice to integrate the INS in the autopilot to reduce the wiring footprint and maintain the same overall form factor of the autopilot. With the advancements of Microelectromechanical Systems (MEMS), INS are increasing in precision and accuracy very rapidly. This being chosen as a modular unit, the INS was not integrated in the Systems Integration Board, as it allows the user to select one that matches the required form factor, the budget allowance and can be easily swapped, if necessary. Also, most of the commercial off the shelf (COTS) navigation sensors come in rugged, self-contained packages which gives freedom to the user to place the unit where it is inconvenient to place the flight control computer. VectorNav's VN-200 Rugged GPS/INS, shown in Figure 14, has been selected as it is a miniature high performance INS that features MEMS inertial sensors, a high-sensitivity GPS receiver, advanced Kalman filtering algorithms to provide optimal estimates of position, velocity and orientation.

Figure 14: VectorNav VN-200 Rugged GPS/INS

Wireless Communication Device: Communication range and reliability are most important factors when the wireless communication device is selected. The Ground Control Station is the relay for all of the relevant information on-board the UAV. Similar to the navigation sensors, wireless communication technology is advancing rapidly and is becoming much more efficient. This component is placed offboard the autopilot, this way it reduces the electromagnetic interference caused by the other systems. The jDrones jD-RF900 Plus Long Range Telemetry set (Figure 15) proved to facilitate the best connection strength and robust.

Figure 15: jDrones jD RF900 Plus

Systems Integration Board (SIB): The main purpose of the SIB (Figure 16) is the integration of the flight control computer with the other sensors and components onboard the aircraft. The SIB was designed with the form factor and robustness in mind.

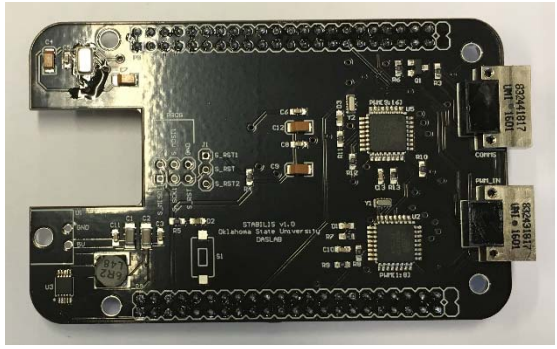

Figure 16: Systems Integration Board

Peripheral Sensors: There were two sensors that have been chosen to go on the SIB. The Honeywell, HSCMRRN001PD2A3, was chosen for its superior resolution, accuracy and form factor to provide the differential pressure reading from the Airspeed sensor. Additionally, we have the Freescale MPL3115A2 Absolute Digital Pressure Sensor on the SIB to provide accurate pressure [Pascal] /altitude [meters] and temperature [^{0}C].

Fail-Safe Servo Driver: The Fail-Safe Servo Driver or Servo Driver (Figure 17) in short, is another important part of the Autopilot Design to guarantee the airborne safety of the small UAV. It is mainly responsible for decoding both piloted and computer generated servo control commands and selecting desired decode signals to drive multiple servo actuators. In case of any malfunction of the any component or accidents during autonomous flight, with the Servo Driver, the human pilot has a chance to retrieve the UAV to safety.

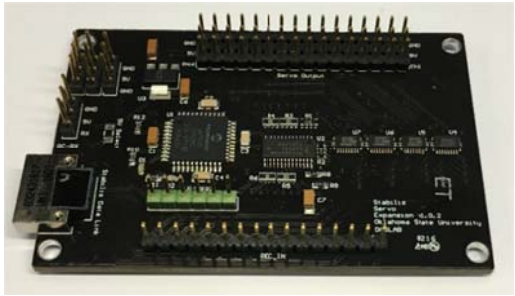

Figure 17: Fail-Safe Servo Driver

2.4.2 Software Design

Operating in the outdoor environment poses the challenge of onboard computation for all control and automation algorithms. Choosing an operating system is one of the most important aspects of the software development in the context of embedded development. The operating system must be light enough to devote most of the processor to core tasks, but minimize development time when trying to perform basic tasks. The following key requirements drove the choice of operating system:

- Tasks must be performed in a deterministic manner
- Operating system must be able to provide precise timing when executing tasks
- Mitigation of low-level, time-consuming programming
- Level of development of the operating system itself

Multi-Threaded Design: The software system for the autopilot is developed based on a multi-threaded architecture to ensure integrity and robustness of the system. The thread structure is employed to execute multiple tasks based on the functionality and hardware components. To

execute the threads, the main() function is initialized with several parameters such as the system gains, actuator limits and sensor profiles. In a multi-threaded system, the tasks for each thread must be scheduled such that the control is executed properly, as shown in Figure 18.

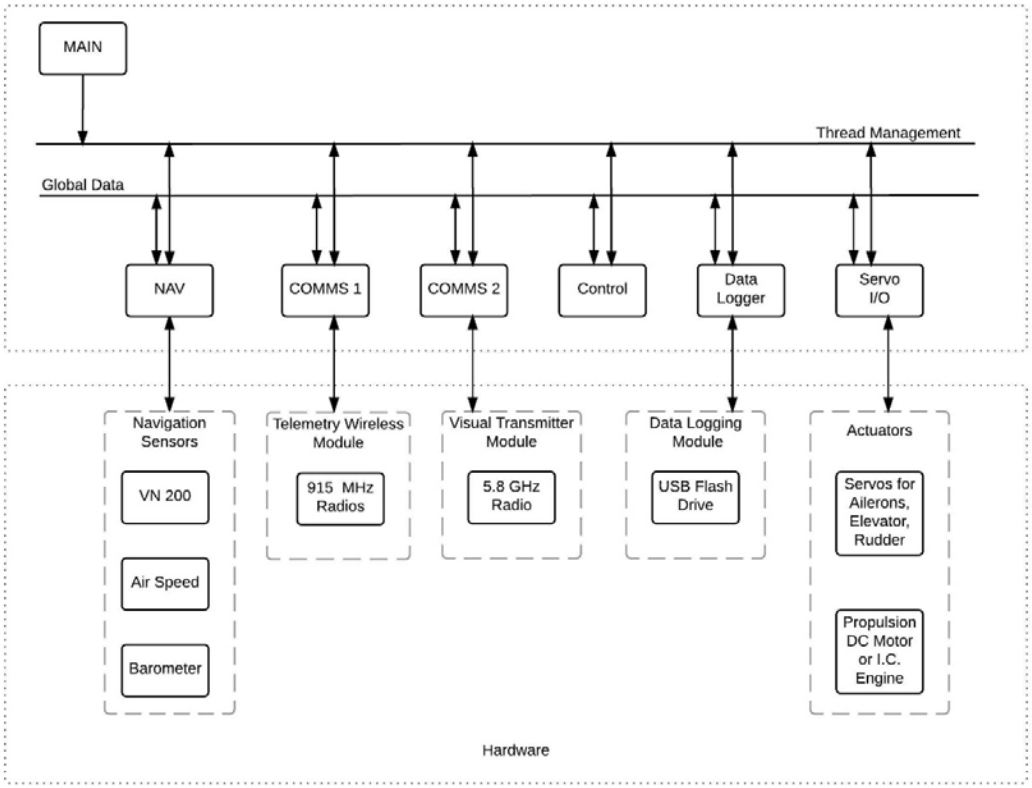

Figure 18: Block Diagram of Thread Design

Ground Control Station Software: The Ground Control Station plays the primary role as the means by which operators plan, execute and monitor UAS missions through a wireless communication channel. The task of the ground station is to provide a realistic interface for users to monitor the performance of the UAV during the flight tests. Many ground control software platforms exist but QGROUNDCONTROL(QGC) is a well-documented, platform independent and community supported ground station software package. QGC software is compatible with the major Operating Systems (Windows, Linux, Mac OS X). It also features serial, UDP, TCP and mesh networks communication compatibility. It also has real-time plotting and logging capabilities of onboard parameters. It also features the ability to change onboard parameters relevant for the Control law. QGC utilizes a highly efficient communication protocol called MAVLINK. MAVLINK is an extensively tested and possibly the most widely used communication protocol in the UAS research community.

2.4.3 GNC Test Aircraft

The SkyHunter (Figure 19) was used as the primary experimental fixed wing platform. The platform is a COTS boom-tail design constructed of though Expanded PolyOlefin (EPO), a good payload bay capable of housing 7 lbs. The high wing design adds a significant amount of stability and robustness in the presence of wind. The aircraft features ailerons and an elevator as control inputs, but no rudder. Other specifications are also provided in Figure 19.

Parameter	Value
Wing Span [mm]	1800
Wing Area [m^2]	0.362
Fuselage Width [mm]	160
Fuselage Height [mm]	150
Fuselage Weight [lb]	9
Engine	DC Motor
Propeller	12x6E

Figure 19: SkyHunter Airframe and Specifications

2.5 GNC and Payload Hardware Integration

GNC and payload hardware integration were also areas of focus during the first half of the program. In addition to providing a complete system capable of true autonomous flight and DAA operations, the VEARAT configuration of BASSET will be a versatile test bed for a vast range of NASA experiments. From modular airframe components to avionics, versatile integration is a paramount objective. To support this purpose, BASSET offers an expansive payload bay of 11 cubic feet. This bay is pictured in

Figure 20, along with an example payload that was flown during the initial test campaign. BASSET offers multiple mounting locations for conventional antennas and communication links. Several skin panels are replaceable, and can be tailored for integrated sensors or RF transparency. A wide variety of onboard power, computing capacity, and programmable I/O for data fusion, recording, and autonomous operations will be available to any hosted payload.

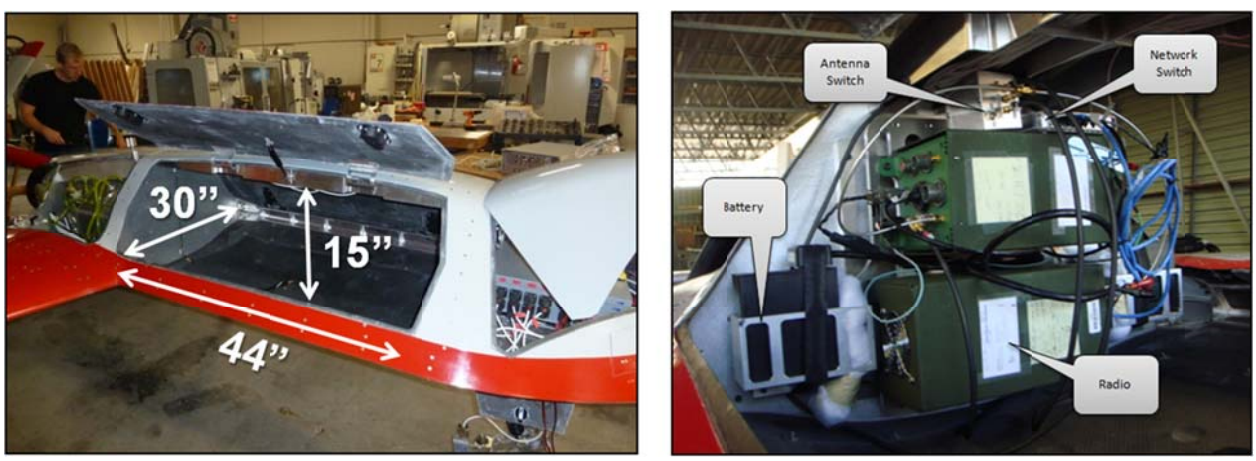

Figure 20: BASSET Payload Bay - Example Integration of an Experimental Radio Payload

Work was conducted to integrate the existing BASSET avionics with the Stabilis systems, and the complete specification of a sensor suite to support DAA flight operations. The baseline BASSET system was composed of a Piccolo II autopilot and peripheral components. While widely used, the Piccolo system is expensive and difficult to integrate with experimental peripherals. As pictured in

Figure 21, the VEARAT avionics suite will feature dual Stabilis cores along with redundant INS sensors. An ADS-B transceiver will be added to coordinate with cooperative aircraft. RTK-GPS will be implemented to achieve the spatial awareness and control resolution necessary for

automated take-off and landings. An LTE modem will also be included to offer an alternate mode of BLOS communication. All of these components will be accommodated with the existing BASSET flight control box. Outside of the flight control box, an Echodyne K-band radar will be installed at the nose of the aircraft. This K-band radar features a metamaterial phased array, which is a game changing technology for radar systems of small UAVs. The metamaterial technology offers reduced size, weight, and power consumption when compared to conventional scanning radar systems. Weighing less than 1 kg and consuming less than 20 watts in operation, this cell phone sized device provides a field of view of +/- 60 degrees in azimuth and +/- 40 degrees in elevation. The concept of integration is shown in Figure 22 and Figure 23.

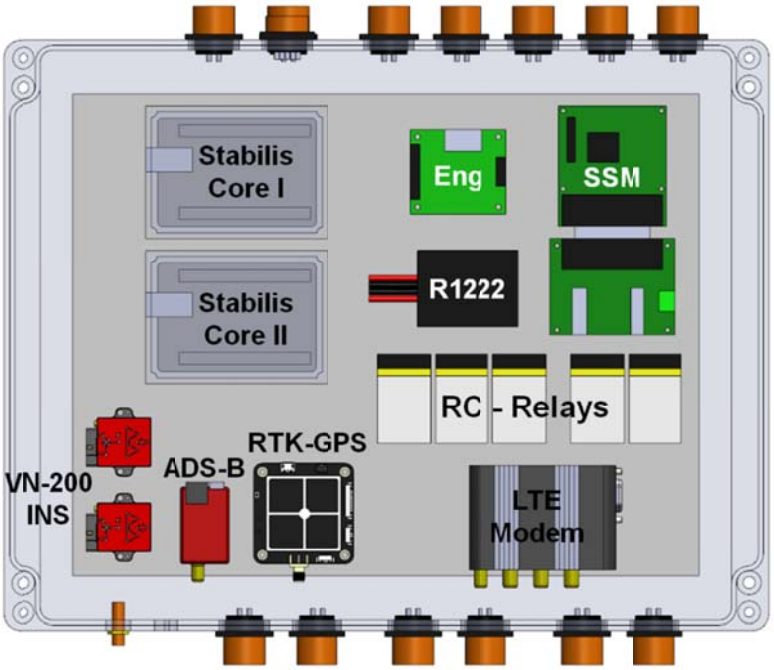

Figure 21: BASSET Flight Control Box - Reconfigured for Stabilis System

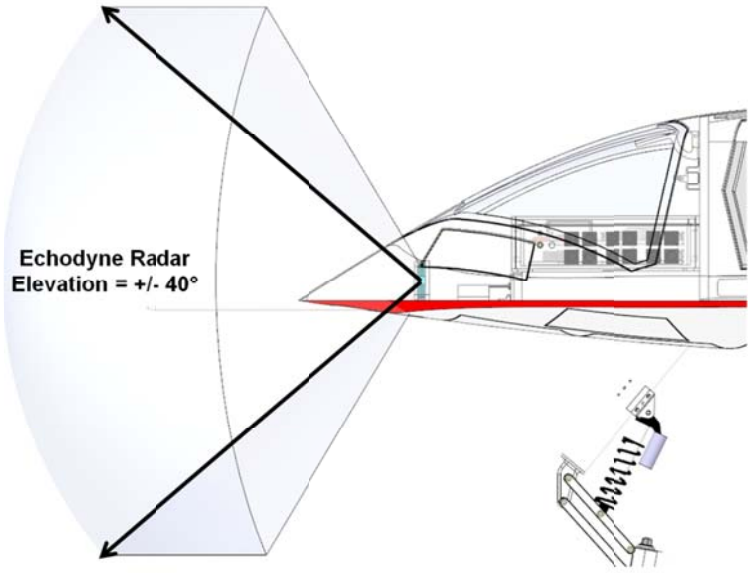

Figure 22: Conceptual Integration of K-band DAA Radar

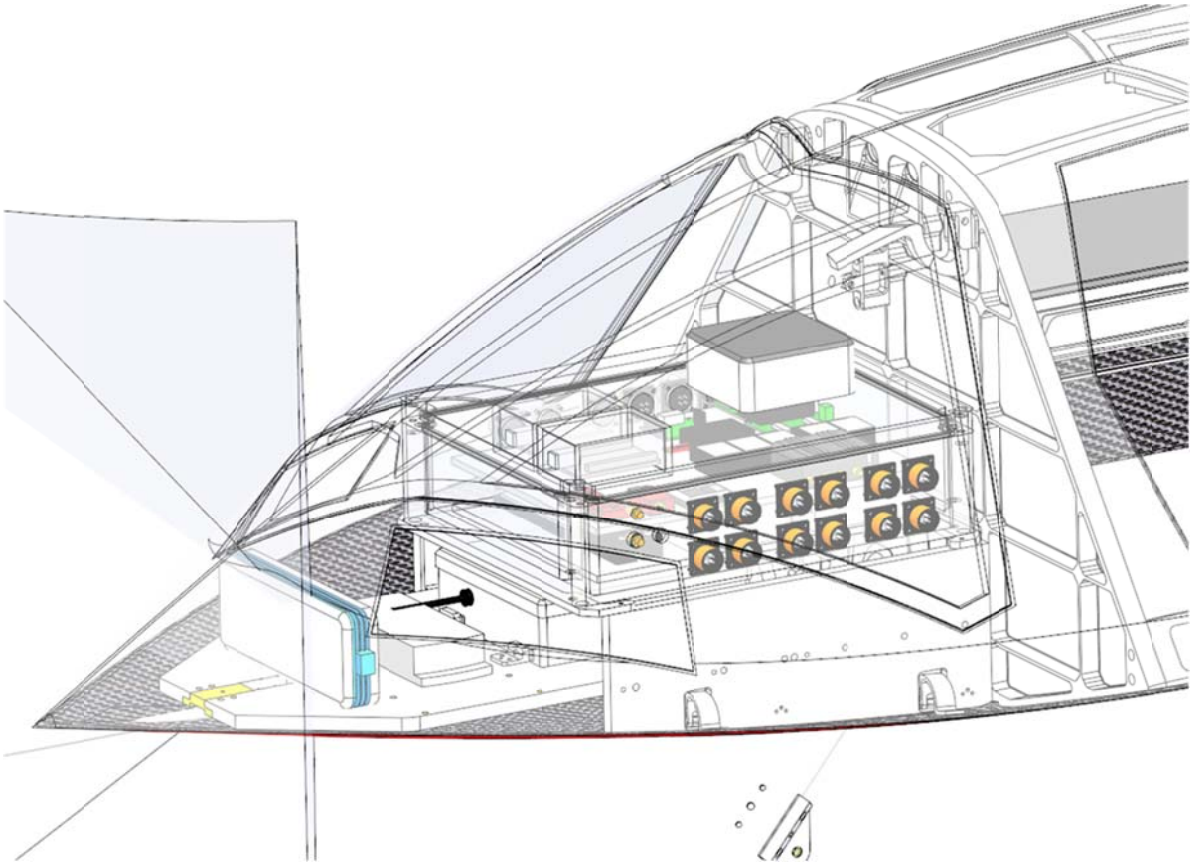

Figure 23: Conceptual Integration of Complete Stabilis DAA System

3 RESULTS AND DISCUSSION

3.1 Propulsion System Aerodynamic Impact Analysis

Increasing span while keeping the original outboard wing OML yielded benefits of structural efficiency, as the modular wing joint was moved outboard to a region with reduced bending moment. Overall wingspan was increased from 22.7' to 25', and a modest improvement in lift/drag (L/D) was noted in subsequent CFD runs.

With any significant change of aerodynamic profile, a check of aircraft stability and performance is warranted. The prior BASSET effort had extensive databases of wind tunnel and CFD runs; therefore the CFD geometries were updated to reflect the changes of the VEARAT configuration. ANSYS CFX was employed to evaluate full Navier-stokes solutions. VEARAT has more wing area and therefore it produces more lift and drag for a given condition (eg Q & AOA). Similarly, VEARAT has a higher aspect ratio wing and therefore we would expect to achieve a higher L/D max than BASSET. A plot of L/D versus angle of attack is shown in Figure 24 for a condition of 55 knots equivalent air speed (KEAS). VEARAT demonstrates higher L/D across the range of 0 to 5 degrees AOA surveyed. The benefit is quite consistent with a value of a 10% improvement. Figure 25 depicts streamline and pressure contour plots of the VEARAT AOA = 2.5 degree case.

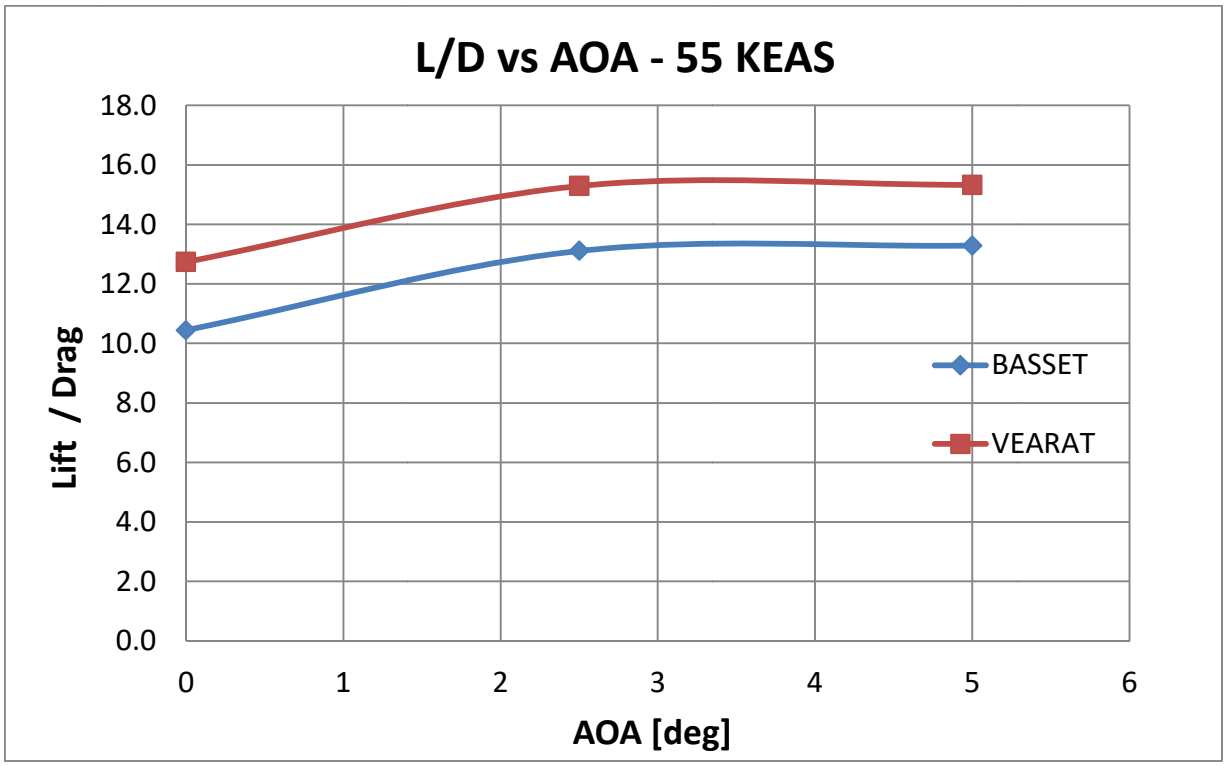

Figure 24: L/D Performance Comparison – BASSET vs. VEARAT

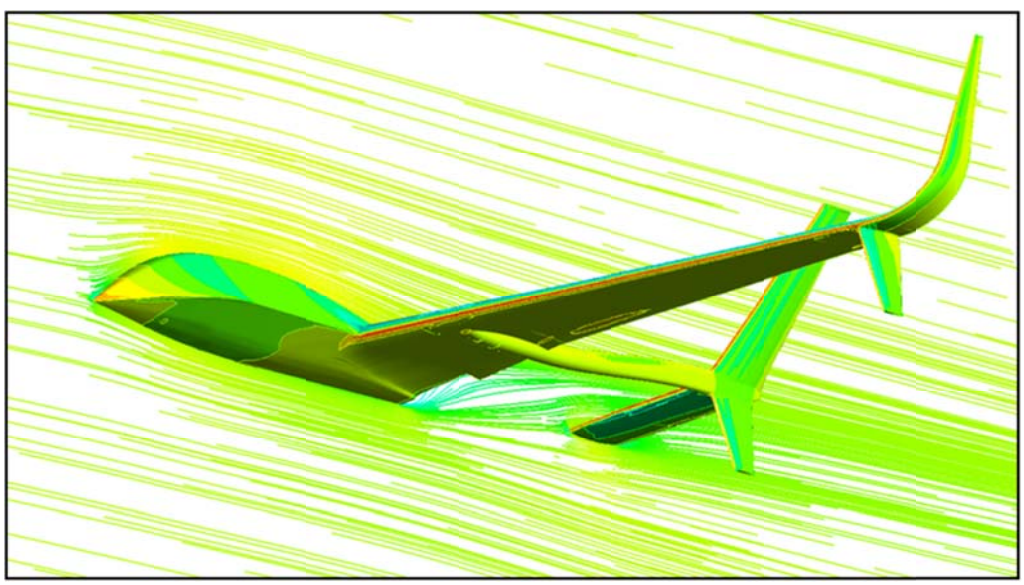

Figure 25: VEARAT - 55 KEAS - AOA = 2.5 - Streamline and Pressure Contour Plots

The VEARAT configuration has approximately 30% more horizontal tail area than BASSET, however the tail quarter chord position is consistent. Wing area was increased 16% with the VEARAT modification. These factors considered, for a given longitudinal CG position VEARAT is more stable or has a higher static margin than BASSET. This fact is evident in Figure 26, and plot of pitching moment coefficient vs. lift coefficient for each configuration. Static margin is 20% higher for the VEARAT configuration. The stick fixed trimmed CL is actually lower for VEARAT, 0.53 vs. 0.76. Given the scope of changes proposed at this time,

specifically how they could affect the vehicle Xcg, we will proceed with this configuration. When a more concrete definition of the payload and overall vehicle inertial properties is available, we can simply adjust the length of the tail booms to achieve the desired stability and optimum trim point.

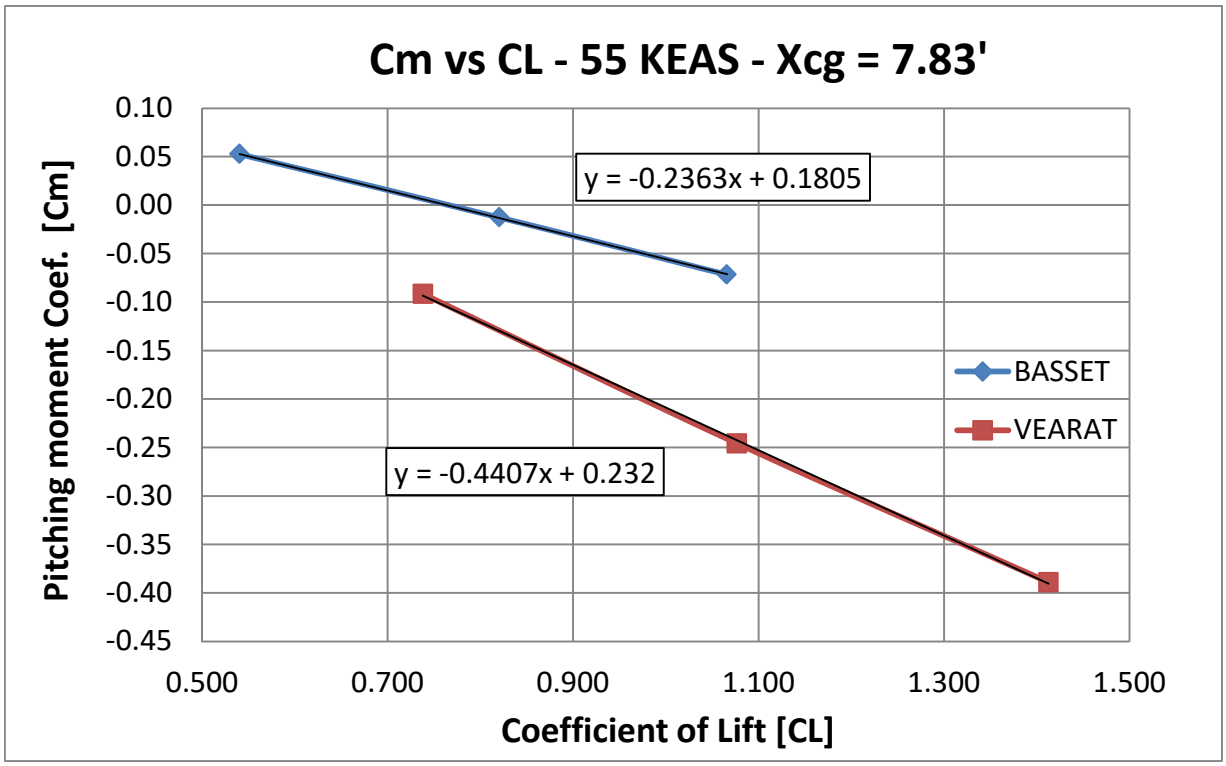

Figure 26: Pitching Moment vs. Lift Coefficient – BASSET vs. VEARAT

3.2 Structural Optimization

3.2.1 Applied Load Distribution for BASSET NASTRAN Wing-box Model

Detailed CFX ANSYS results were post-processed to obtain point loads at various sections along the span. These point loads matched the total lift and moments of the detailed CFD model. However, application of point loads led to stress concentration along the span. Thus, an equivalent pressure distribution was developed for the wing-box region of the upper and lower skin which could match the force and moments experienced by the wing-box due to the CFD pressure distribution shown in Figure 27. This led to much more uniform application of applied loads and avoided erroneous local stresses.

The wing-box skin lied between 15% (front spar) to 70% (rear spar) of the wing and thus forms 55% of the total wing area. The pressure distribution in this region was matched to generate 55% of the total wing lift obtained from CFD and also match the location of the center of pressure obtained from the CFD analysis to ensure accurate pitching moments. Half-span lift for a 3.35 g load case from the adjusted pressure distribution amounted to 768.57 lbf. The lift for the equivalent region obtained from the FD analysis amounted to 757 lbf. The validation is shown for one test section along the span marked with an arrow in Figure 27. The center of pressure obtained from the CFD results at the test section is shown in Figure 28. This can be compared to the location of center of pressure along the span shown in Figure 29 as obtained from the adjusted pressure distribution.

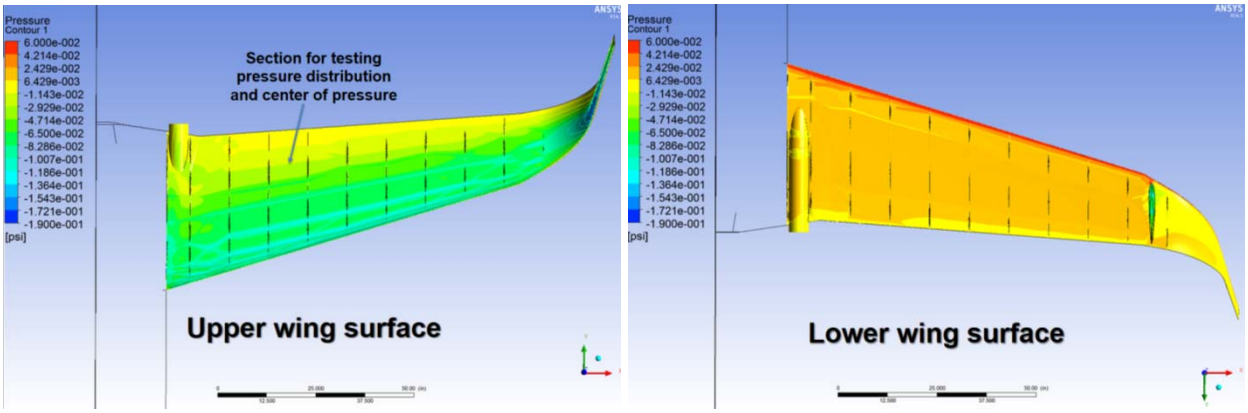

Figure 27: CFD Pressure Distribution

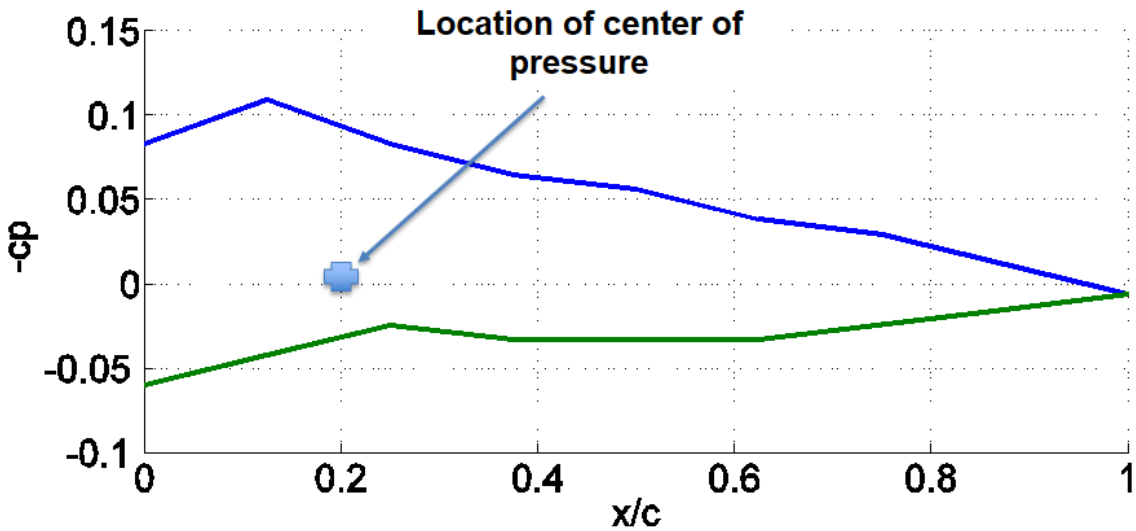

Figure 28: Pressure Distribution at Test Section

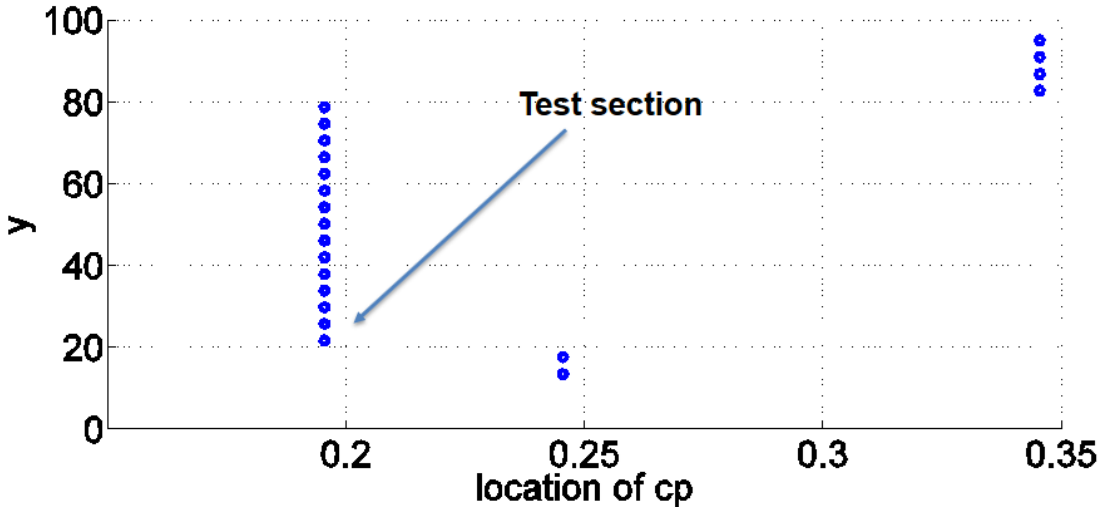

Figure 29: Location of Center of Pressure along the Span

The matched pressure distribution was applied to the NASTRAN skin elements. The forces at the winglet were applied as point forces distributed over the outboard section where the wing is connected to the winglets. Point masses due to the winglet and the outboard aileron were modeled with CONM2 elements in NASTRAN. These point masses as well as the mass of the structure, were factored with the corresponding acceleration for the load case via the GRAV card in NASTRAN which can incorporate the acceleration in terms of *g*. The applied forces are shown in Figure 30. Fixed boundary conditions were applied at the location where the wing spars enter the bulkhead receptacle.

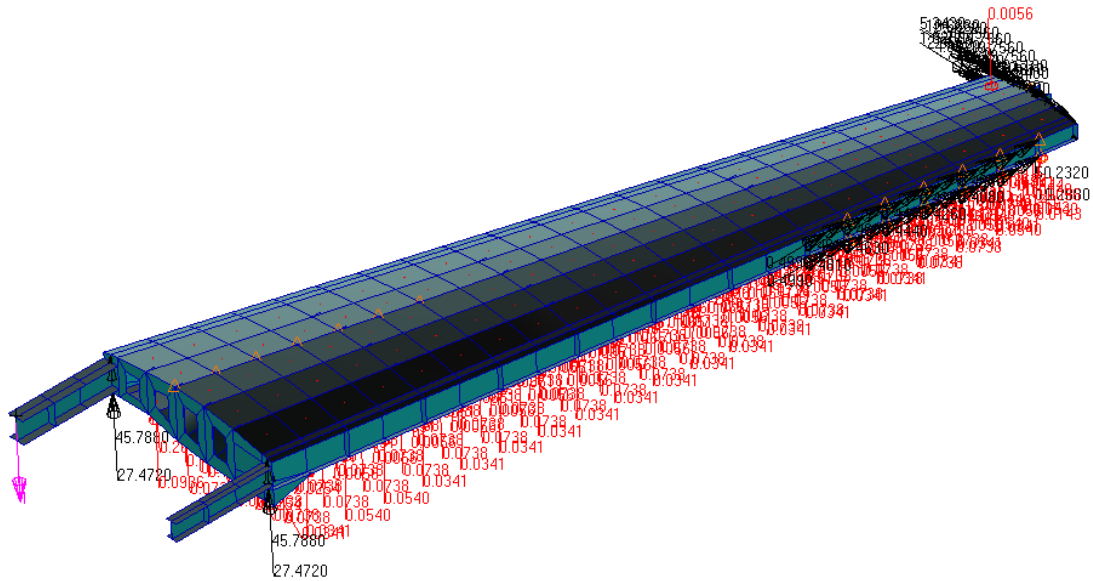

Figure 30: Applied Forces

3.2.2 BASSET Wing Optimization Results

The design optimization study was performed using the SOL 200 module in NASTRAN. The SOL 200 uses a gradient-based optimizer IPOPT. IPOPT implements an interior point line search filter method to find a local optimum for large scale nonlinear optimization.

The load case was *3.35g* pull-up case for which the aerodynamic forces were obtained from the CFD analysis. The existing BASSET vehicle was used as a baseline for comparison of the optimized weight. The optimization results are shown in Figure 31. The optimized wing-box weighed 16.33 lbs., which is 55% lower than the baseline weight. The constraint satisfaction used the following equation for computing the constraint,

$$\boldsymbol{constraint} = (\boldsymbol{von\ Mises\ stress} \times \boldsymbol{safety\ factor} - \boldsymbol{yield\ strength})/\boldsymbol{yield\ strength}$$

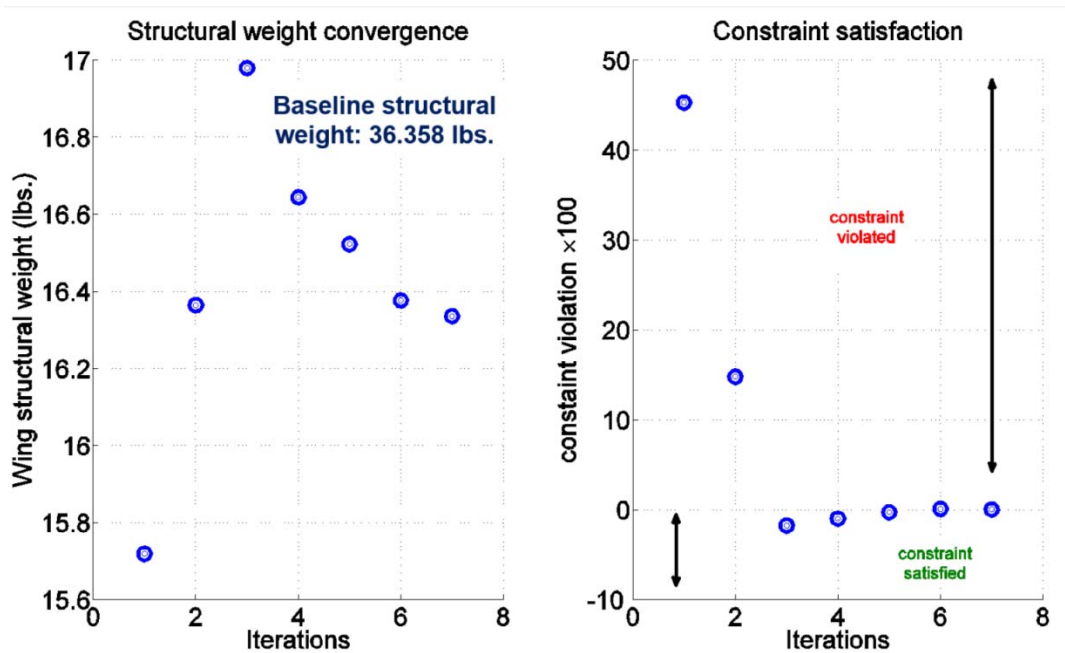

Figure 31: BASSET Optimization Results for 3.35 g Load Case

The stress distribution at various stages of the optimization process is shown in Figure 32. The stress initially increases locally and often reaches beyond the allowable stress as the optimizer tries to reduce the structural weight by reducing the thickness of the designed members. This is reflected by an increase in constraint violation in Figure 31. However, eventually an optimum solution is reached where the von Mises stress constraint is satisfied. The constraint activity is shown in Figure 33. One can see that the constraints are active mainly in the root spar where the structure is subjected to the maximum bending and shear stresses.

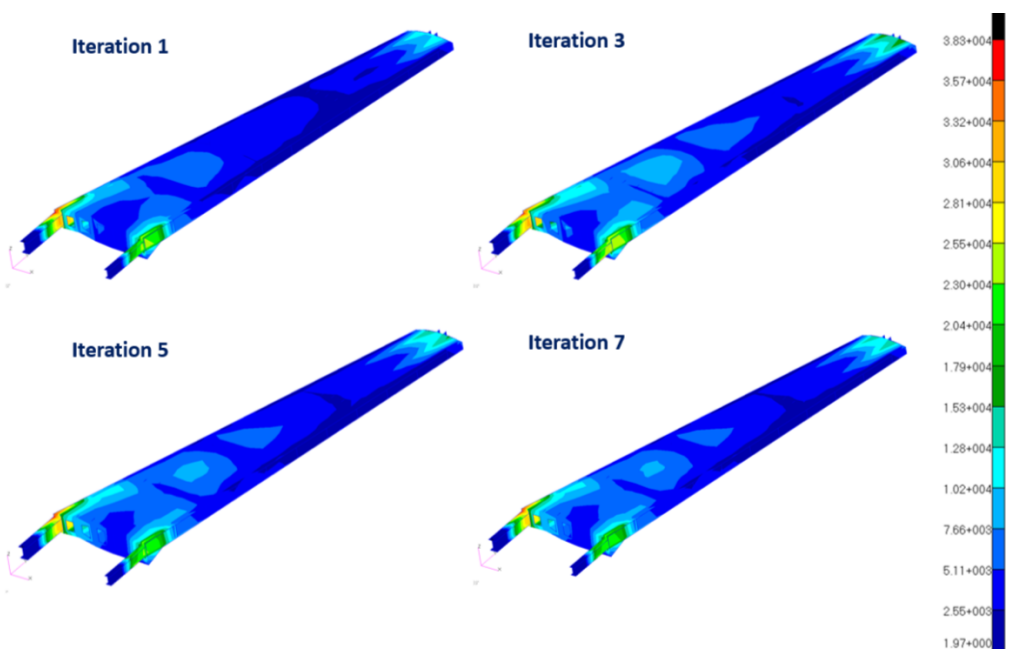

Figure 32: Stress Distribution: BASSET Optimization for 3.35 g Load Case

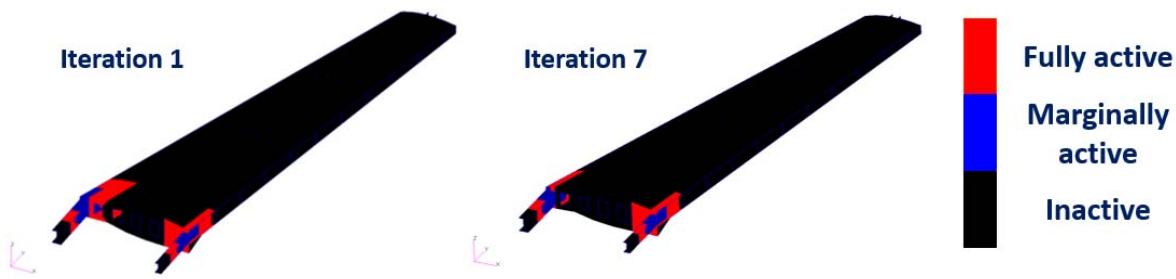

Figure 33: Constraint Activity - BASSET Optimization for 3.35 g Load Case

The thickness distribution along the span for the various designed members is shown in Figure 34. The thickness decreases along the span starting from the root as a result of the reduced bending and shear stresses. The increase in thickness again at the tip is due to the local stresses generated by the forces from the winglet. From Table 3, one can see that the weight for each section reduced significantly resulting in an overall reduction of 55% of the wing-box weight of the baseline vehicle. The only increase in weight is observed in the skin. However, this is mainly due to replacing the composite skin by an aluminum skin for the design optimization study. Replacement of the present skin by a composite skin is expected to further reduce the weight of the wing-box.

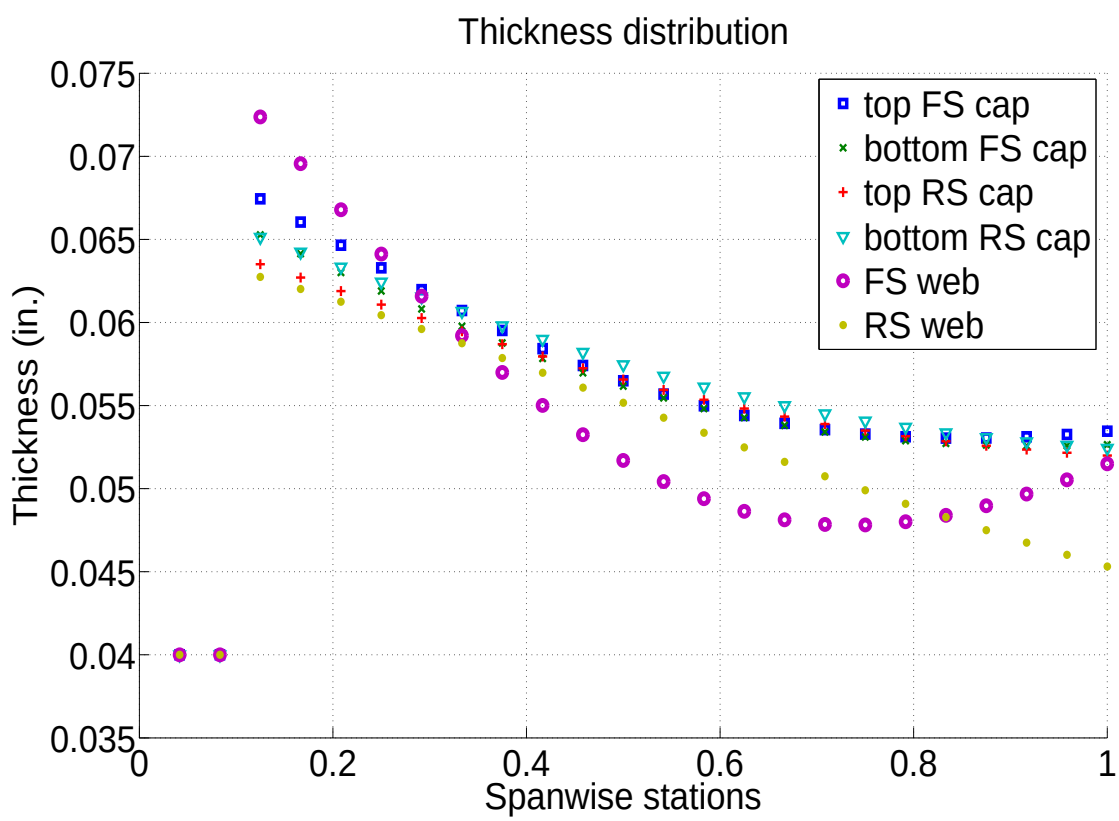

Figure 34: BASSET Optimized Thickness Distribution, 3.35 g Load Case

Table 3: Comparison of Member Weight

Member weight	Baseline	Optimized	% Change
Front spar (lbs.)	14.861	3.6133	-75.686
Rear spar (lbs.)	7.159	2.7635	-61.398
Skin (lbs.)	6.035 (composite)	7.1000 (Al 7075-T6)	17.644
Ribs (lbs.)	8.303	2.8858	-65.569
Total (lbs.)	**36.258**	**16.3356**	**-55.07**

Another design optimization was conducted to observe the effects of performing a more aggressive maneuver with the present BASSET vehicle. This load case is a *5 g* pull-up maneuver. The aerodynamic loads as well as the inertia loads were scaled accordingly and the design optimization study was conducted. The optimization results are compared to the *3.5 g* case design optimization in Figure 35. The results showed that inclusion of the aggressive pull-up resulted in only a 5% increase in the weight of the wing-box and the overall weight of the wing-box was still 50% lower than the baseline weight.

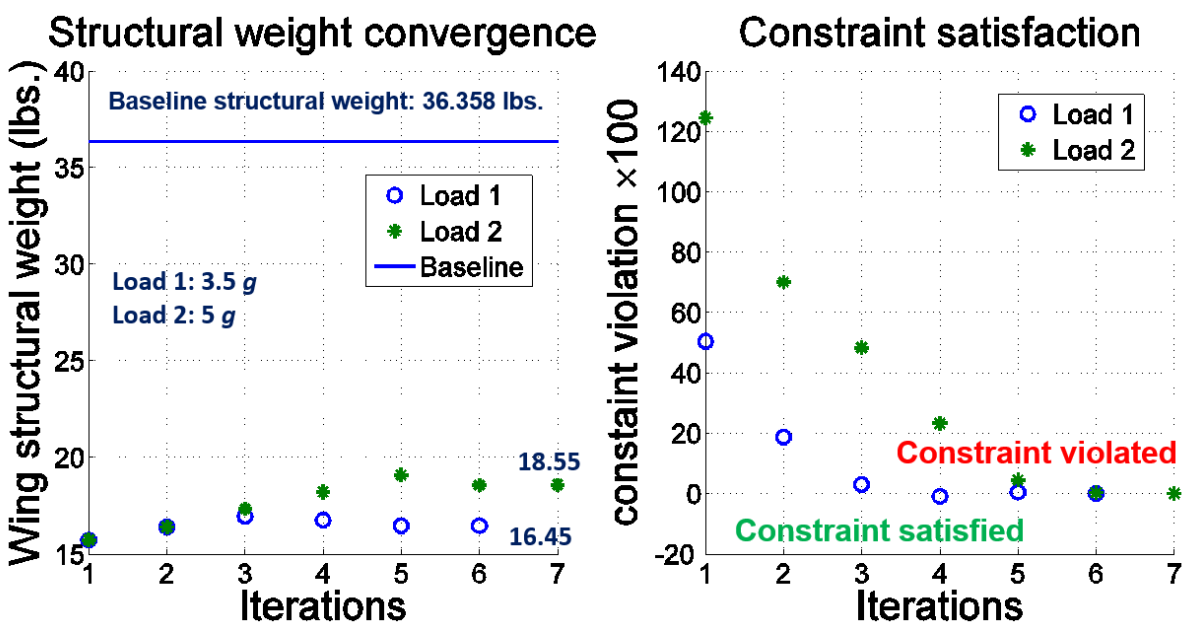

Figure 35: Comparison of BASSET Optimized Results, 3.35 g and 5 g

A buckling check was also performed as a part of post-optimization analysis, and the design was found to be safe from buckling.

3.2.3 Applied Loads on VEARAT

The CFD pressure distribution of the upper and lower skin of the VEARAT configurations is shown in Figure 36. As explained earlier, the pressure distribution on the PSHELL elements of the FEM is adjusted from 55% of the overall lift of the CFD pressure distribution and also matches the location of the center of pressure along the span. The adjusted pressure distribution formed an overall lift of 1058 lbs. compared to the 1100 lbs. lift due to CFD pressure distribution. The adjusted pressure distribution on the upper skin, lower skin and the location of the center of pressure along the span is shown in Figure 37, Figure 38, and Figure 39 respectively.

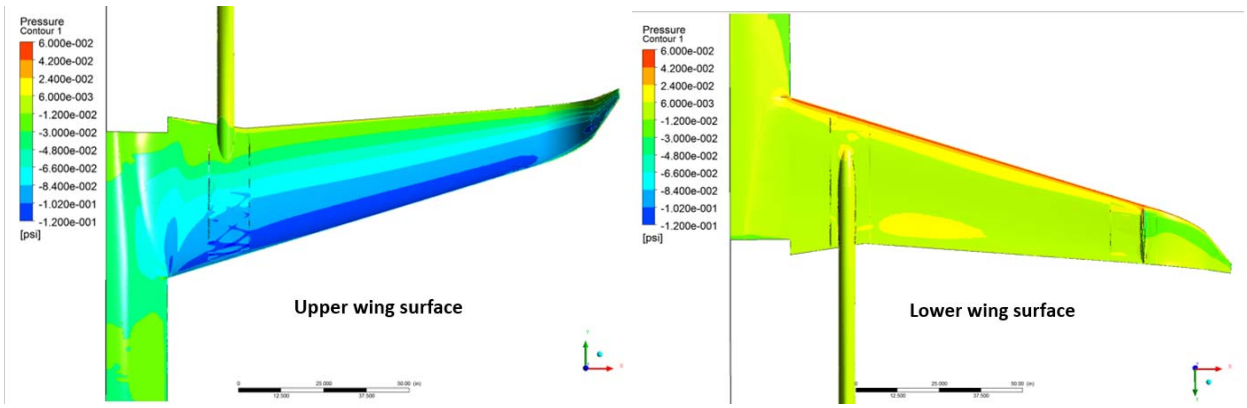

Figure 36: CFD Pressure Distribution on Upper and Lower Skins

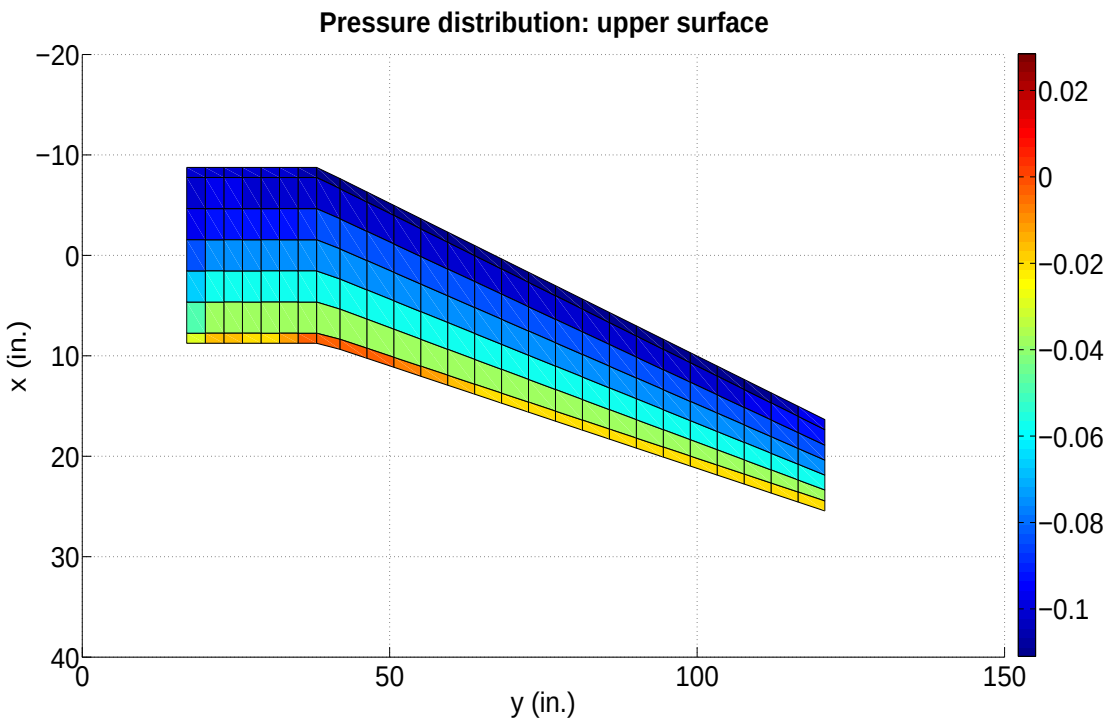

Figure 37: Adjusted Pressure Distribution on the Upper Skin

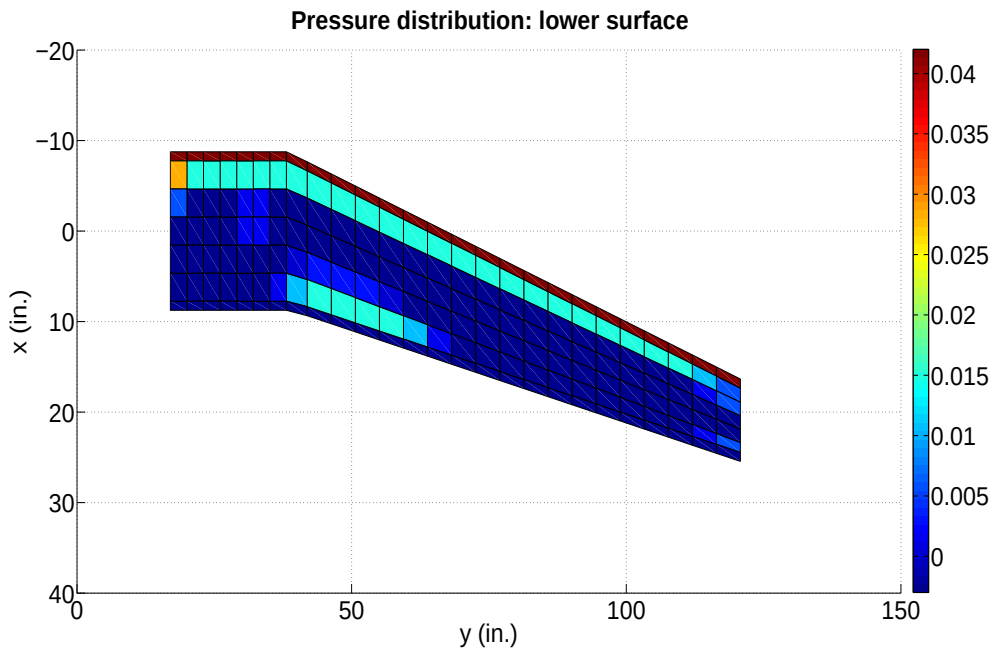

Figure 38: Adjusted Pressure Distribution on the Lower Skin

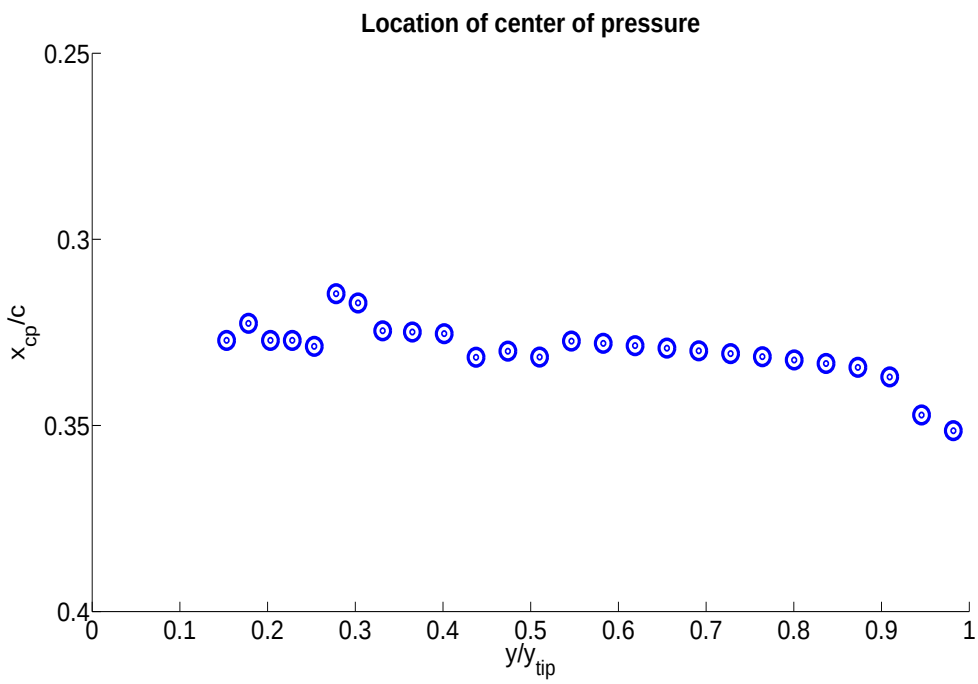

Figure 39: Location of Center of Pressure along the Span

The mass of the structure along with those of the ailerons are factored with the acceleration of vehicle to form the inertia forces. Another force that has been considered here are the forces coming from the tail via the tail booms during a dive condition. These are shown by the yellow point forces at the inboard trailing edge in Figure 40. These forces are grouped in a separate load case to be used for the optimization of the vehicle.

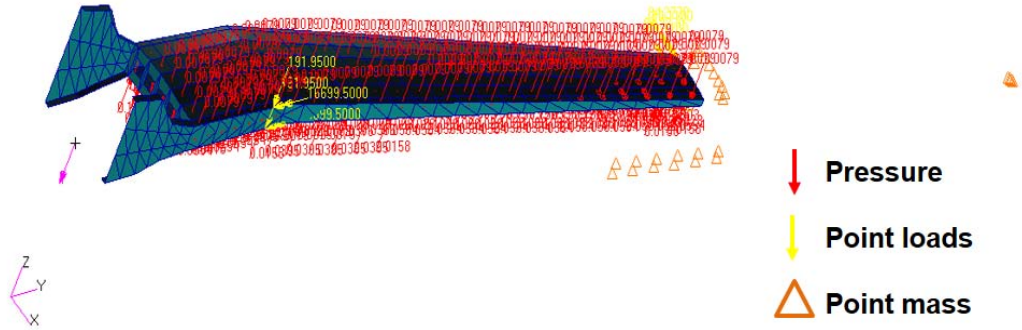

Figure 40: Applied Loads on VEARAT FEM

3.2.4 VEARAT Wing Optimization Results

For a better understanding of the physics, we look at the stress distribution of Case 2 for the individual load cases during several cycles of the optimization. Two load subcases are considered:

Load Subcase 1 – Aero loads for 3 g pull-up + inertia loads due to structural weight, aileron weight (Figure 41)

Load Subcase 2 – Same as before + max Q dive case (tail loads transferred to wing) (Figure 42)

The optimization was performed for two subcases. One can see that for Load Subcase 1, the higher von Mises stresses are observed at the root spar, with the highest being at the forward spar. However, the stress distribution does not change much after iteration 4. This is expected as the Load Subcase 1 by itself requires 3 cycles of optimization as shown by Subcase 1 from Figure 43. For Load Subcase 2, several iterations are required to satisfy the stress constraint at the tail boom-wing intersection due to the tail loads. This explains the much higher number of cycles required for Subcase 2 to converge. The results for the optimization are shown in Figure 43 for both the cases.

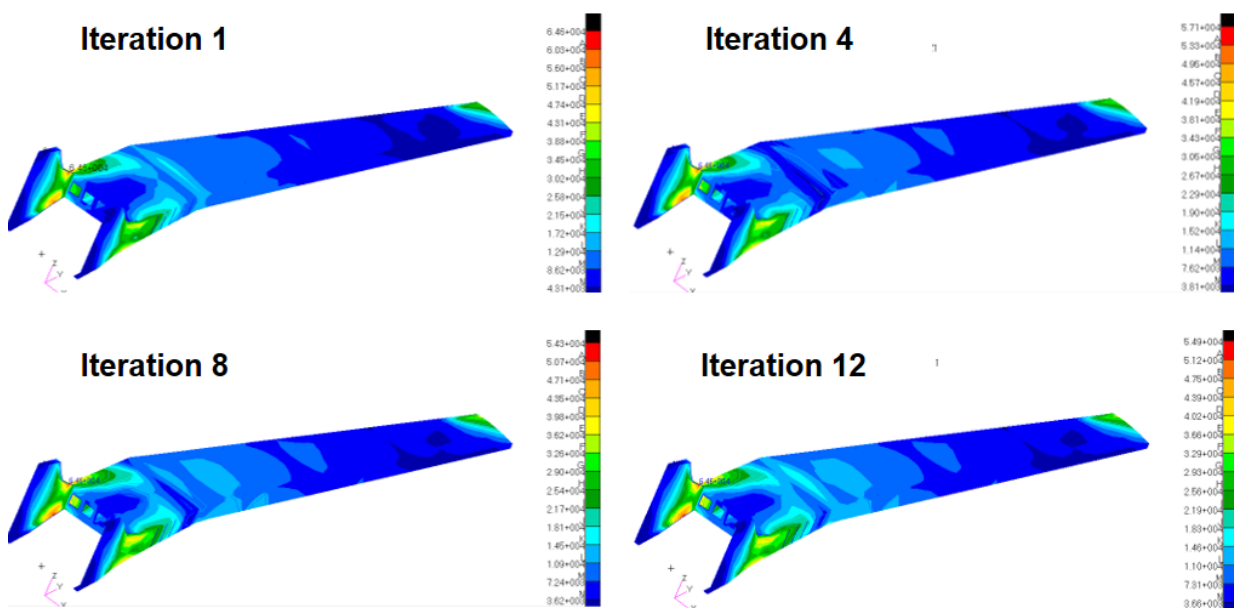

Figure 41: Stress Distribution - Load 2, Load Subcase 1

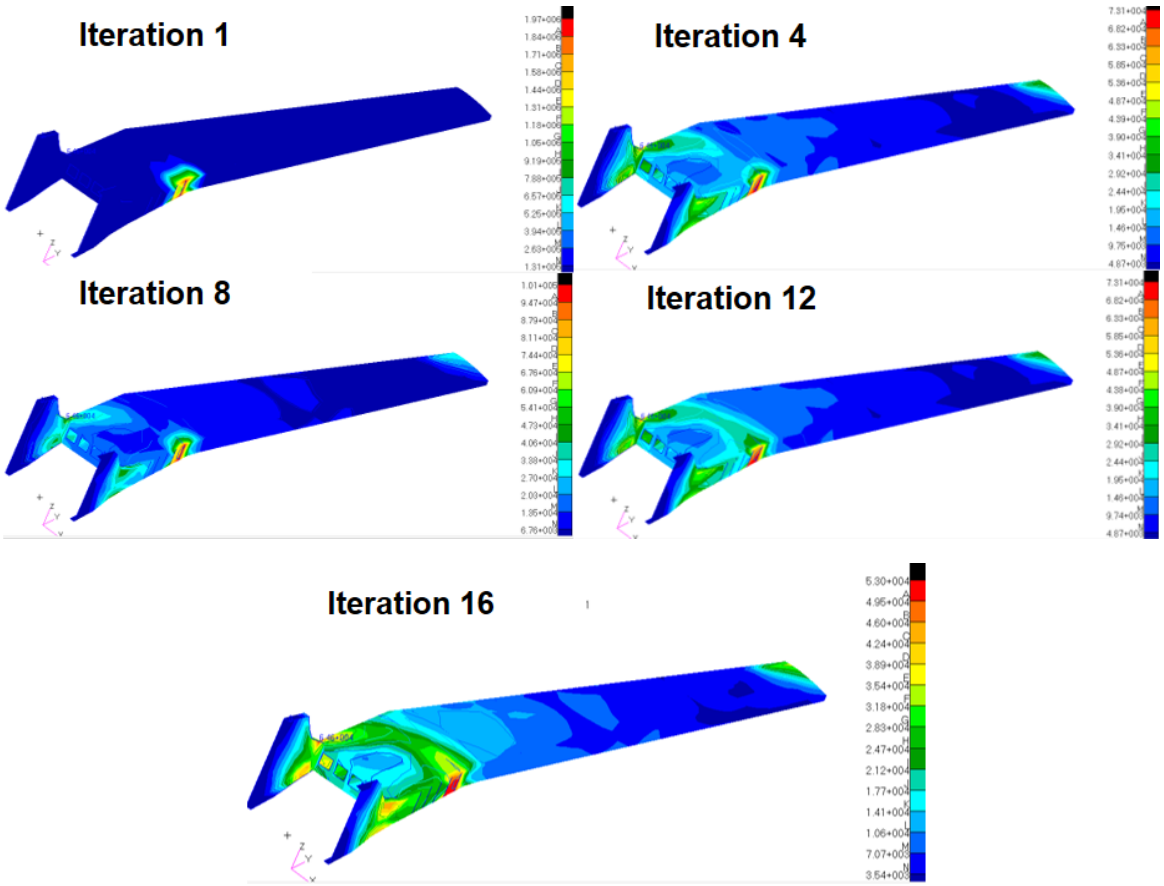

Figure 42: Stress Distribution - Load 2, Load Subcase 2

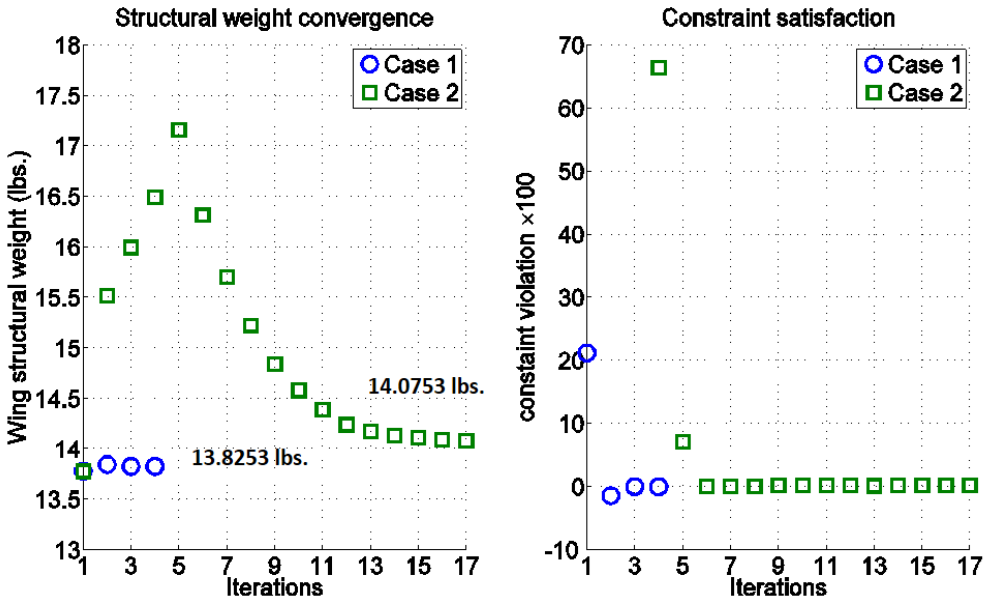

Figure 43: VEARAT Structural Optimization Results

Looking at the thickness distribution of the various spar sections along the span in Figure 44, it is evident that the thickness of the rear spar caps and especially the rear spar web at the intersection of the tail boom and the wing are increased to carry the tail loading. This explains for the 0.25 lbs. increase in the wing weight for Subcase 2.

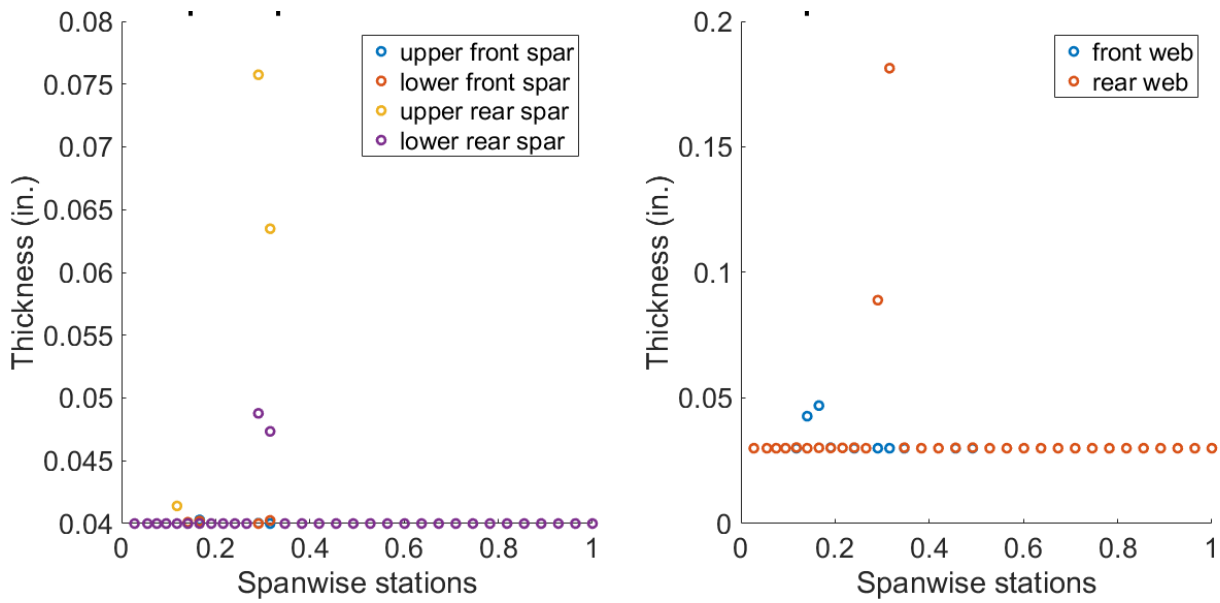

(a) (b)

Figure 44: VEARAT Load Case 2 Optimized Member Thickness (a) Spar Cap and (b) Spar Web

3.2.5 FEM Optimization Conclusions

The study aimed to reduce the weight of the structural wing-box BASSET UAV via optimization. First, the BASSET configurations were studied and a NASTRAN FEM was developed based on the CAD model. Then, adjusted pressure distribution for the FEM was developed based on the CFD results for the BASSET configurations. Subsequent optimization studies showed that 55% of the wing-box weight could be saved via structural optimization. Even an aggressive *5 g* load case required almost 45% lower weight than the baseline design.

A similar optimization study performed for the refined VEARAT configurations predicted similar wing-box weights for the optimized design. However, inclusion of a load case which applied the tail loads during dive into the optimization led to a small increment in the structural weight owing to the thickening of the spar web and the spar caps at the intersection of the tail boom and the wing.

Future studies recommended for this project would be investigation of the wing-box structural response in presence of gust loads, and optimal mass placement in presence of strong gusts.

3.2.6 CAD Modeling of FEM Optimized Wing Structure

The result of the FEM optimization of the wing structure results in new shell element thickness for the skins, spars, ribs, and stiffeners. The FEM is a simplification of the actual wing structure that does not include the additional details required for manufacture. To determine the actual weight and mass distribution of the optimized wing structure the new element thickness were used to model in SolidWorks the full wing assembly. The result of this wing modeling is shown in Figure 45.

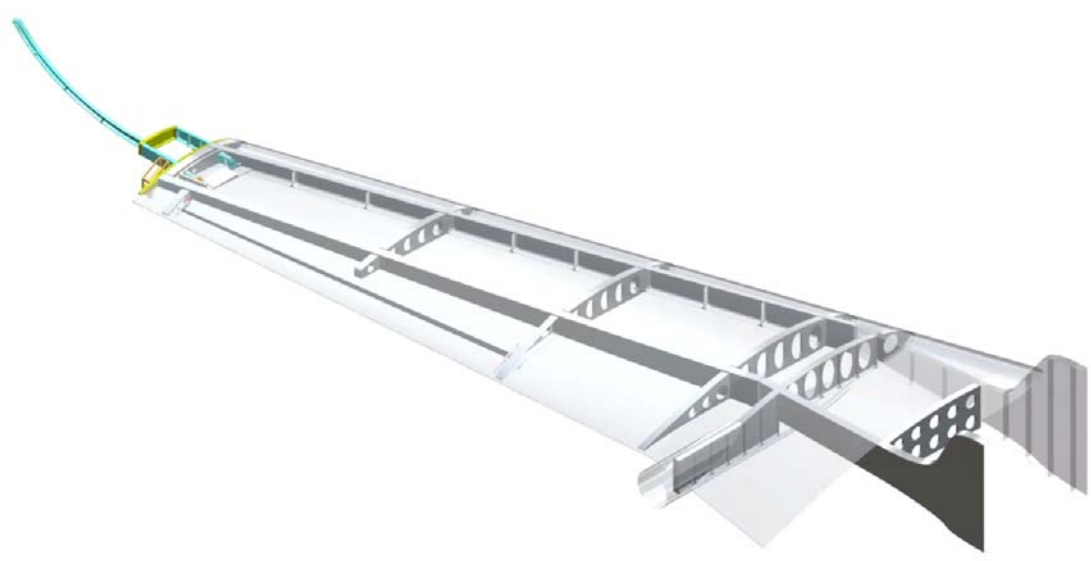

Figure 45: Detail Designed Optimized VEARAT Wing Structure

The wing structure shown in Figure 45 is based on the optimized FEM models but includes the additional features such as ailerons, lap joints, fillets, and stiffeners required to manufacture an actual wing. The wing CAD model was cut into a number of smaller sub pieces for which the mass and inertia properties were extracted. The mass distribution is shown in Table 4 and the location points are shown in Figure 46. These distributed masses could be used in the future to conduct gust load analyses.

Table 4: Mass Distribution of Detail Designed Optimized VEARAT Wing Structure

#	X	Y	Z	Mass [lb]	Moments of inertia: (pounds * square inches),Taken at the center of mass, aligned with the output coordinate system.								
1	-7.2	4.3	88.2	2.66	Lxx = 27.749	Lxy = 7.541	Lxz = -0.047	Lyx = 7.541	Lyy = 23.945	Lyz = 0.014	Lzx = -0.047	Lzy = 0.014	Lzz = 51.513
2	-7.0	3.2	105.4	2.02	Lxx = 12.150	Lxy = 4.311	Lxz = 0.156	Lyx = 4.311	Lyy = 15.371	Lyz = 0.005	Lzx = 0.156	Lzy = 0.005	Lzz = 27.433
3	-23.7	0.5	83.3	0.71	Lxx = 7.978	Lxy = 0.301	Lxz = -1.325	Lyx = 0.301	Lyy = 13.664	Lyz = 0.491	Lzx = -1.325	Lzy = 0.491	Lzz = 11.426
4	-20.9	1.2	96.3	4.18	Lxx = 213.535	Lxy = 2.360	Lxz = -3.412	Lyx = 2.360	Lyy = 268.010	Lyz = -0.120	Lzx = -3.412	Lzy = -0.120	Lzz = 93.985
5	-24.0	-0.3	114.7	1.38	Lxx = 41.987	Lxy = 0.123	Lxz = 1.199	Lyx = 0.123	Lyy = 55.357	Lyz = -6.392	Lzx = 1.199	Lzy = -6.392	Lzz = 20.414
6	-37.1	0.0	85.9	0.80	Lxx = 4.267	Lxy = 0.406	Lxz = -2.930	Lyx = 0.406	Lyy = 15.083	Lyz = 0.172	Lzx = -2.930	Lzy = 0.172	Lzz = 13.860
7	-38.2	0.3	97.1	9.65	Lxx = 571.443	Lxy = -0.484	Lxz = -5.287	Lyx = -0.484	Lyy = 640.267	Lyz = 12.323	Lzx = -5.287	Lzy = 12.323	Lzz = 109.681
8	-36.2	-0.8	114.3	3.59	Lxx = 113.573	Lxy = -2.157	Lxz = 7.144	Lyx = -2.157	Lyy = 137.827	Lyz = -6.704	Lzx = 7.144	Lzy = -6.704	Lzz = 46.687
9	-49.8	-0.4	89.2	0.39	Lxx = 1.767	Lxy = 0.133	Lxz = -1.703	Lyx = 0.133	Lyy = 6.725	Lyz = 0.051	Lzx = -1.703	Lzy = 0.051	Lzz = 6.188
10	-49.8	0.2	99.6	1.20	Lxx = 80.418	Lxy = 0.850	Lxz = -6.953	Lyx = 0.850	Lyy = 100.521	Lyz = 1.397	Lzx = -6.953	Lzy = 1.397	Lzz = 34.348
11	-49.7	-0.6	114.9	1.14	Lxx = 20.692	Lxy = 0.360	Lxz = -2.304	Lyx = 0.360	Lyy = 35.400	Lyz = -2.886	Lzx = -2.304	Lzy = -2.886	Lzz = 17.975
12	-63.7	-0.7	93.6	0.52	Lxx = 2.240	Lxy = 0.140	Lxz = -2.127	Lyx = 0.140	Lyy = 8.019	Lyz = 0.073	Lzx = -2.127	Lzy = 0.073	Lzz = 7.074
13	-63.9	-0.2	103.1	2.95	Lxx = 105.209	Lxy = 1.026	Lxz = -8.106	Lyx = 1.026	Lyy = 133.326	Lyz = 1.507	Lzx = -8.106	Lzy = 1.507	Lzz = 41.208
14	-63.7	-0.9	116.9	1.38	Lxx = 17.335	Lxy = 0.398	Lxz = -2.147	Lyx = 0.398	Lyy = 33.648	Lyz = -2.303	Lzx = -2.147	Lzy = -2.303	Lzz = 18.929
15	-76.0	-1.0	97.2	0.38	Lxx = 1.583	Lxy = 0.128	Lxz = -1.665	Lyx = 0.128	Lyy = 6.561	Lyz = 0.047	Lzx = -1.665	Lzy = 0.047	Lzz = 5.893
16	-75.9	-0.5	106.3	1.70	Lxx = 49.537	Lxy = 0.615	Lxz = -6.043	Lyx = 0.615	Lyy = 69.414	Lyz = 0.558	Lzx = -6.043	Lzy = 0.558	Lzz = 27.390
17	-75.9	-1.1	118.8	0.94	Lxx = 8.989	Lxy = 0.237	Lxz = -1.858	Lyx = 0.237	Lyy = 21.579	Lyz = -1.151	Lzx = -1.858	Lzy = -1.151	Lzz = 13.897
18	-89.8	-1.3	101.5	0.51	Lxx = 1.971	Lxy = 0.127	Lxz = -1.919	Lyx = 0.127	Lyy = 7.407	Lyz = 0.075	Lzx = -1.919	Lzy = 0.075	Lzz = 6.419
19	-89.8	-0.9	109.7	2.43	Lxx = 59.721	Lxy = 0.694	Lxz = -6.487	Lyx = 0.694	Lyy = 84.090	Lyz = 0.687	Lzx = -6.487	Lzy = 0.687	Lzz = 31.272
20	-89.1	-1.3	120.4	0.82	Lxx = 5.696	Lxy = 0.144	Lxz = -1.242	Lyx = 0.144	Lyy = 16.579	Lyz = -0.705	Lzx = -1.242	Lzy = -0.705	Lzz = 11.717
21	-102.3	-1.6	105.3	0.38	Lxx = 1.472	Lxy = 0.122	Lxz = -1.644	Lyx = 0.122	Lyy = 6.487	Lyz = 0.049	Lzx = -1.644	Lzy = 0.049	Lzz = 5.737
22	-102.2	-1.1	113.0	1.44	Lxx = 28.285	Lxy = 0.445	Lxz = -4.992	Lyx = 0.445	Lyy = 45.898	Lyz = 0.289	Lzx = -4.992	Lzy = 0.289	Lzz = 21.642
23	-102.0	-1.6	122.4	0.62	Lxx = 2.782	Lxy = 0.137	Lxz = -1.230	Lyx = 0.137	Lyy = 11.418	Lyz = -0.342	Lzx = -1.230	Lzy = -0.342	Lzz = 9.058
24	-116.9	-1.9	109.8	0.49	Lxx = 2.128	Lxy = 0.162	Lxz = -2.788	Lyx = 0.162	Lyy = 10.143	Lyz = 0.067	Lzx = -2.788	Lzy = 0.067	Lzz = 8.800
25	-117.2	-1.5	116.6	1.95	Lxx = 29.837	Lxy = 0.810	Lxz = -7.252	Lyx = 0.810	Lyy = 63.706	Lyz = 0.282	Lzx = -7.252	Lzy = 0.282	Lzz = 37.376
26	-115.4	-1.8	124.1	0.57	Lxx = 1.384	Lxy = 0.087	Lxz = -0.815	Lyx = 0.087	Lyy = 8.100	Lyz = -0.167	Lzx = -0.815	Lzy = -0.167	Lzz = 6.934
27	-125.1	-0.9	117.7	2.34	Lxx = 63.063	Lxy = -50.396	Lxz = -44.035	Lyx = -50.396	Lyy = 193.443	Lyz = 16.274	Lzx = -44.035	Lzy = 16.274	Lzz = 181.232

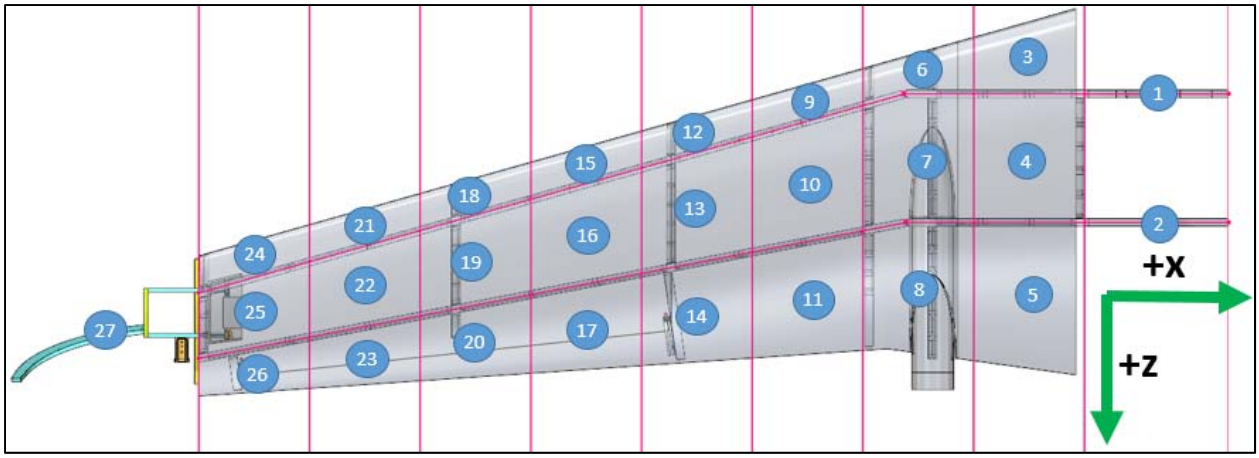

Figure 46: Location of Mass Distribution Points

3.2.7 VEARAT Mass Savings

As described in the previous sections, the wing mass calculated by FEM showed a reduction of 55%, but is not fully representative of the wing if it were manufactured with all the additional brackets and fasteners. With the detailed designed CAD model with the actual features ready for manufacture, a more accurate analysis of weight savings can be made compared to the originally manufactured BASSET wing. The results of the detailed designed wing mass savings are presented in Table 5.

Table 5: Detail Design Wing Structural Weight Savings after Optimization

	BASSET	VEARAT	% Savings
Wing Weight [lb] (both wings)	120.0	68.2	43%

As described the expected mass savings of a manufactured VEARAT wing is approximately 43%. This is the result of structural load optimizing and the conversion from a prototype manufacturing technique to a quasi-production technique.

As most of the aircraft was manufactured under similar methods, this amount of weight savings can be applied to other areas of the aircraft. The predicted VEARAT aircraft weight is seen in Table 6.

Table 6: Projected VEARAT Structural Weight Savings

Project Total Vehicle Structural Weight Savings [lb]
139.1

	BASSET	VEARAT	% Savings
Fuselage weight [lb]	91.6	52.0	43%
Tail weight [lb]	42.3	24.0	43%
Landing gear weight [lb]	68.1	38.7	43%

The predicted VEARAT aircraft structural weight is approximately 139 lbs. The weight saved by the reduction of structural mass will be converted to the heavier, more efficient engine as well as additional fuel to increase the aircraft endurance. The aircraft endurance results are presented in Table 7.

Table 7: VEARAT Vehicle Endurance Enhancements

Endurance Enhancement	
New Engine Added Mass [lb]	86.5
New Fuel Capacity [us Gal]	14.3
Flight Time [hr]	**6.2**

The reduction of aircraft structural mass and the addition of a more fuel-efficient engine has resulted in a 6 hour flight endurance, which matches design goals.

3.3 GNC Flight Test Results

Primarily we have conducted flight tests to demonstrate the performance of the autopilot with three main goals:

- Stabilized flight
- Autonomous way point guidance
- Autonomous landing and takeoff

To validate the design and test for any potential autopilot software flaws we adopted the testing philosophy of flight in simulated environment prior to actual flights. XPlane Simulator by Laminar Research is used to simulate aircraft dynamics in order to evaluate the autopilot. The following test philosophy is adopted for testing the autopilot system,

- Software in Loop (SIL)
- Hardware in Loop
- Flight tests

The controller parameters that proved to be successful in simulations are used in flight-testing. Although the simulation model was accurate, the learning rate in adaptive loop took some tuning, because of clock difference from simulations to flight computer. The following tests were carried out and results are presented in the subsequent section of the document.

- Manual Flight
- Assistive Stable Flight
    - Onboard Adaptive controller tracks the stick command of pilot and assists pilot in achieving stable flight
- Autonomous Flight
    - Complete autonomous flight with onboard Way-point Guidance Algorithm
- Stall Recovery
- Autonomous Landing

3.3.1 Stable Flights

Stable flight or Assistive stable flight, tracks the stick command of the pilot and when there are no inputs from the pilot, the controllers bring the plane from its current attitude to zero stable attitude hold. This mode provides the flexibility to any novice pilot to safely fly the airplane. Stable mode is also designed with saturation on the attitude angle and rates the vehicle can

achieve, thereby limiting the excursion on the performance and facilitating stable and safe flight. Figure 47, Figure 48, and Figure 49 show the aircraft performance in stable mode. The roll and pitch attitude of the vehicle track the commanded roll and pitch respectively and in absence of any command the aircraft is returned to zero attitude hold mode.

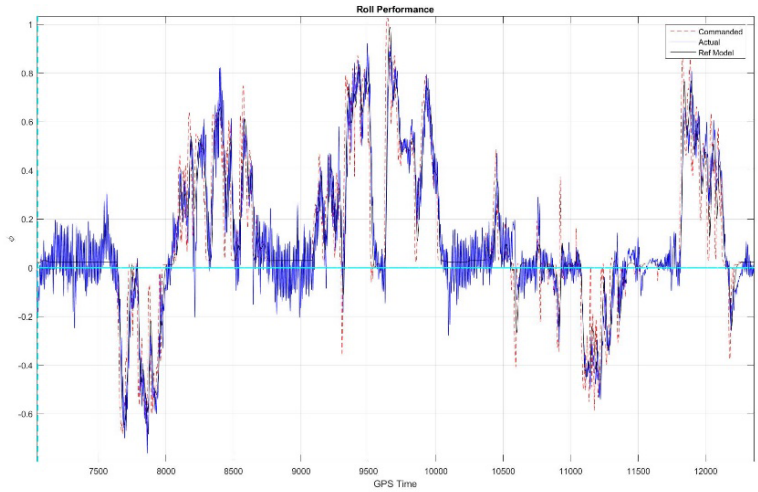

Figure 47: Stable Flight, Tracking Performance of Aircraft to Commanded Roll

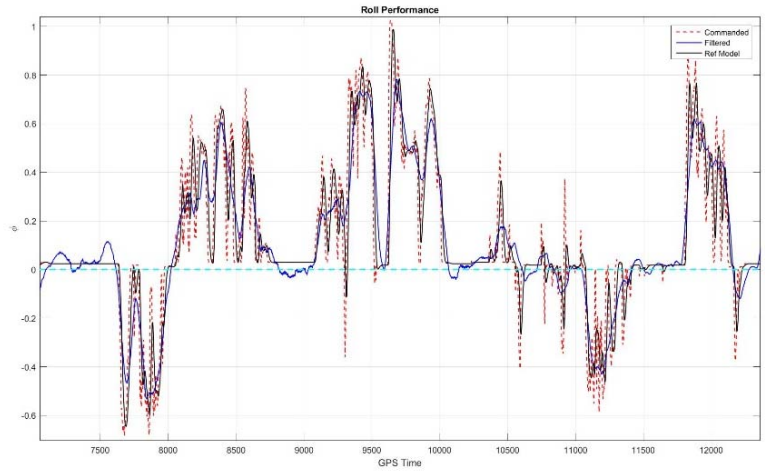

Figure 48: Stable Flight, Tracking Performance of the Aircraft to Commanded Roll: Post Flight Filtered Data

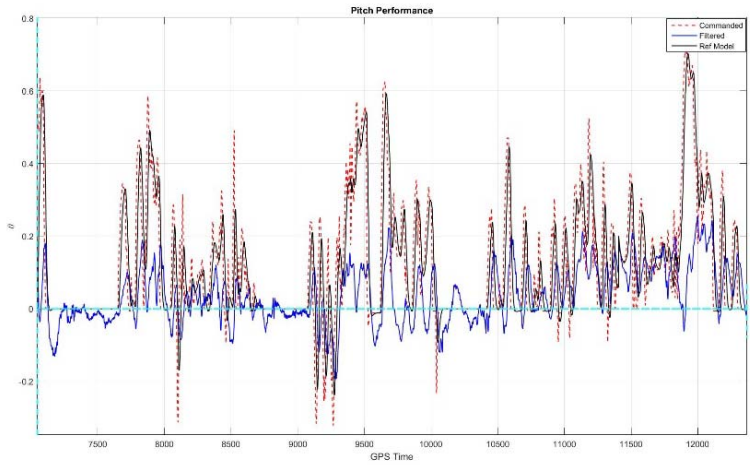

Figure 49: Stable Flight, Tracking Performance of the Aircraft to Commanded Pitch: Post Flight Filtered Data

3.3.2 Autonomous Waypoint Guidance

In this section, flight test results are presented for aircraft autonomously tracking 8 waypoints arranged in a stretched hexagonal pattern. All of the flight tests were performed at OSU's Unmanned Aircraft Flight Station. In Figure 50, the red-dots denote the commanded waypoints, the dotted line connecting the dots denotes the path the aircraft is expected to take, except while turning at the way points. While turning at the way points, the onboard guidance law smooths the trajectory with circles of 80 feet radius. The deviation of the trajectory from the desired trajectory is due to heavy cross wind. During the day of flight, the wind disturbances experienced on the course ranged between 20 to 30 knots. For an aircraft of the size of SkyHunter with 10lbs total weight, 30knots of cross wind is a significant external disturbance. Also, the aircraft flight tested is a rudderless plane, hence its heading correction capability in presence of heavy cross wind is limited due to actuator deficiency. Yet under a high disturbance scenario, the adaptive control performed well and achieved the required stable flight and handling. The aircraft was able to achieve the desired waypoint tracking. Figure 50 shows the ground track for the autonomous flight in waypoint guidance. Figure 51 and Figure 52 shows the time plot for roll and pitch attitude of the vehicle to track the commanded waypoints.

Figure 50: Autonomous Waypoint Guidance: STABILIS Autopilot on Skyhunter Flight Test

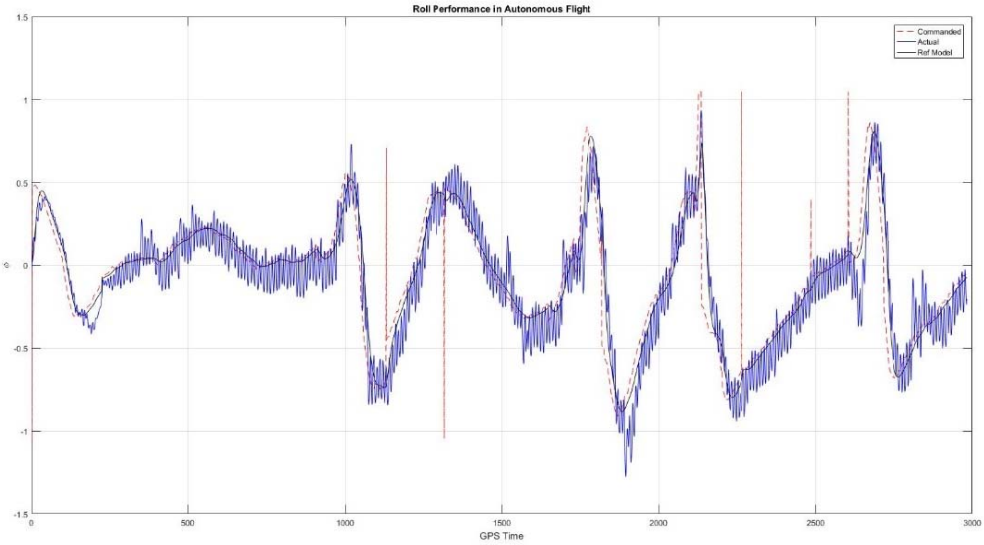

Figure 51: Commanded Roll Attitude Tracking for Autonomous Waypoint Guidance

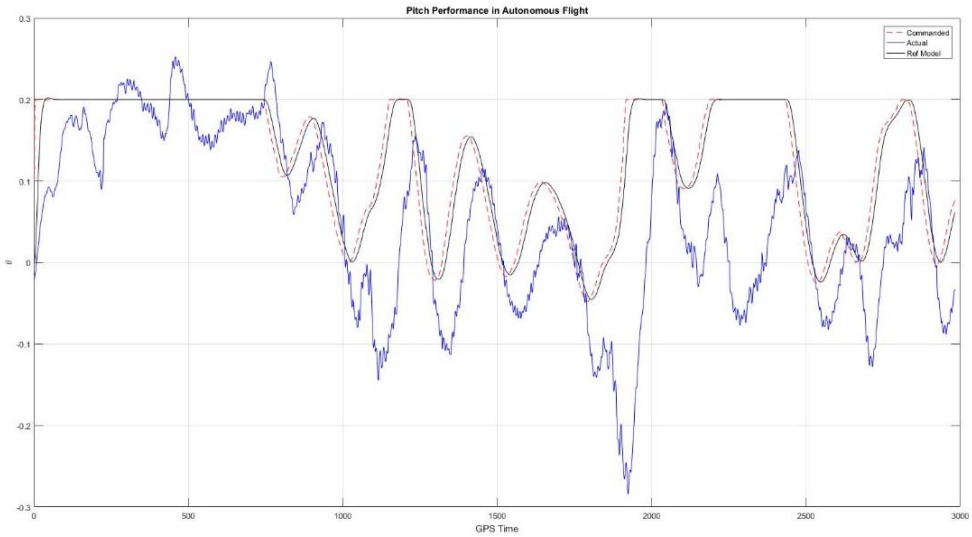

Figure 52: Commanded Pitch Attitude Tracking for Autonomous Waypoint Guidance

To validate and test the waypoint guidance code, the autonomous flight was simulated in the HIL setup as well before actual flight test. This flight test in HIL was mostly with ideal condition testing. No cross wind simulated, this exercise is done to test the code integrity and controller parameters tuning. Figure 53 shows the ground track of the aircraft executing waypoint tracking. Figure 54 and Figure 55 show commanded and achieved roll and pitch attitude of vehicle to perform the trajectory tracking. Under nominal conditions, the controller is demonstrated to achieve very close tracking of the desired trajectory, and flight results shows the robustness of the code to unknown extreme disturbance.

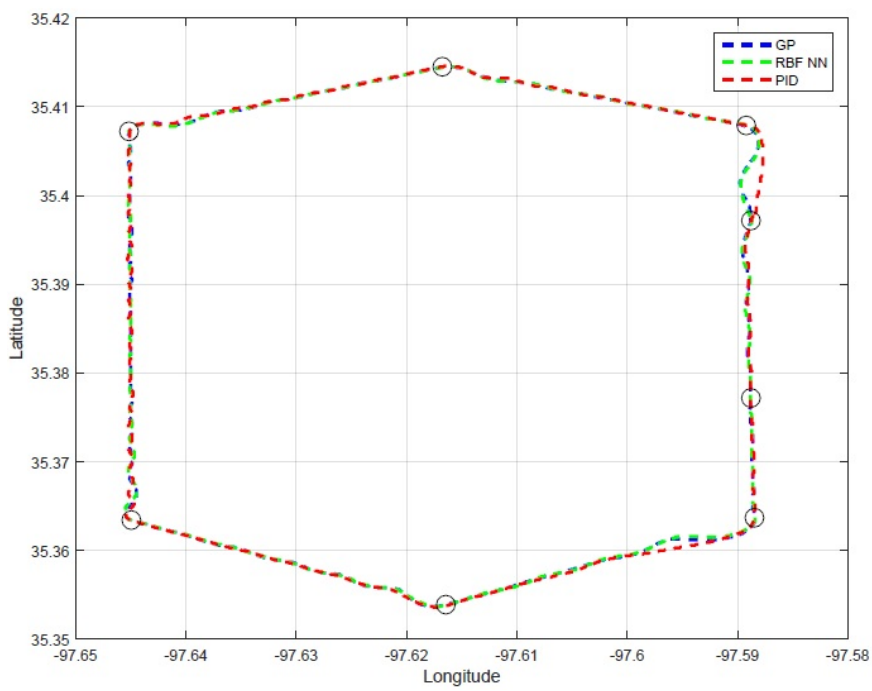

Figure 53: Autonomous Waypoint Guidance - STABILIS Autopilot on SkyHunter, HIL Test (No Cross Wind)

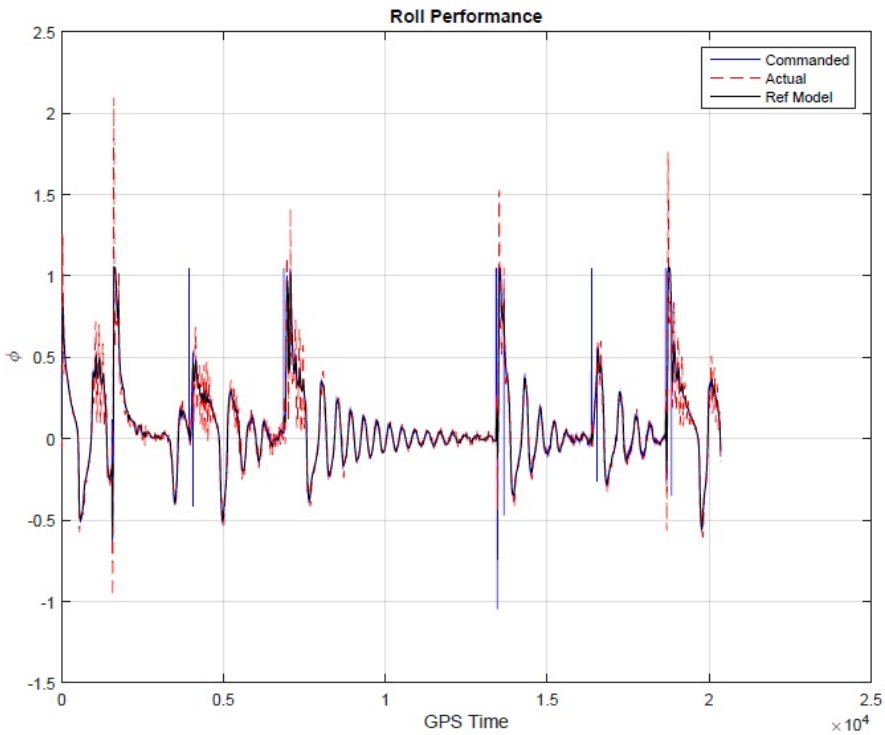

Figure 54: Commanded Roll Attitude Tracking for Autonomous Waypoint Guidance - HIL Test (No Cross Wind)

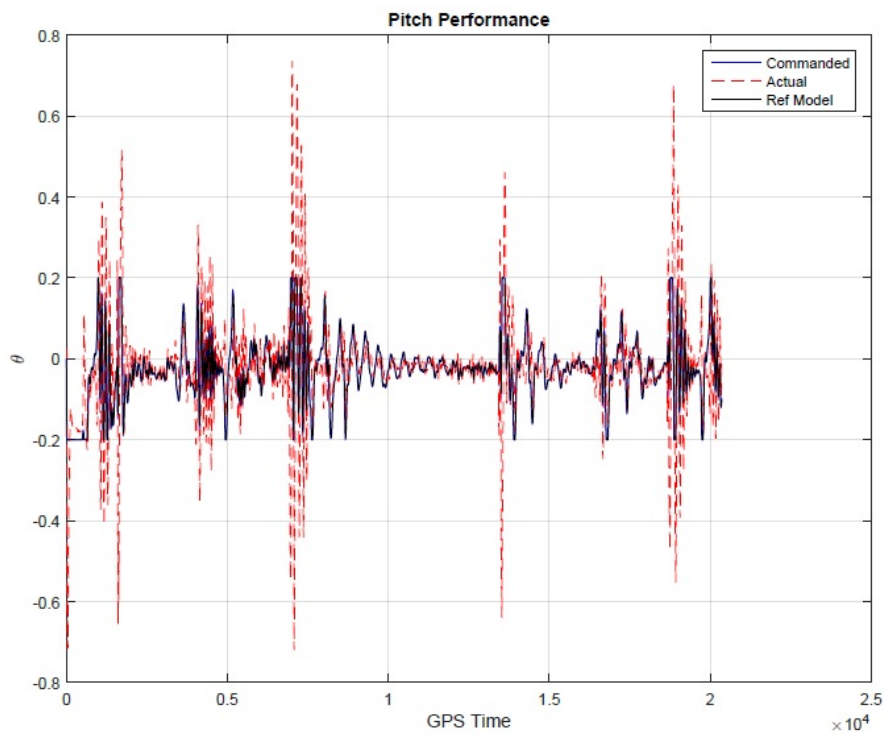

Figure 55: Commanded Pitch Attitude Tracking for Autonomous Waypoint Guidance - HIL Test (No Cross Wind)

Stall Recovery: A stall recovery maneuver was flight tested, to validate the autopilot capability to recover aircraft from extreme flight conditions and achieve a stable flight. The aircraft was maneuvered to a high pitch angle achieving high angle of attack at which the aircraft lost lift. At this point the UAV motor was also switched off, killing off the thrust. The stable mode of the autopilot demonstrated its ability to recover the UAV from stall at zero throttle. Figure 56 and Figure 57 show pitch and roll performance in stall recovery.

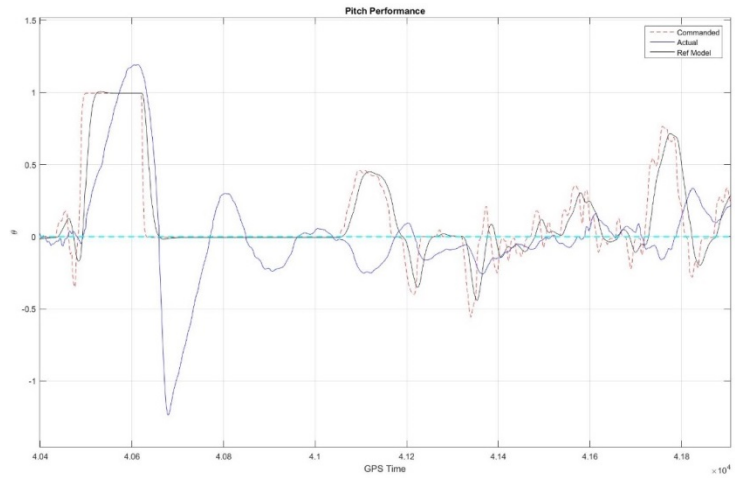

Figure 56: Stall Recovery Maneuver - UAV Pitch Attitude demonstrating Stall, Loss of Lift and Altitude, and Recovery Phase

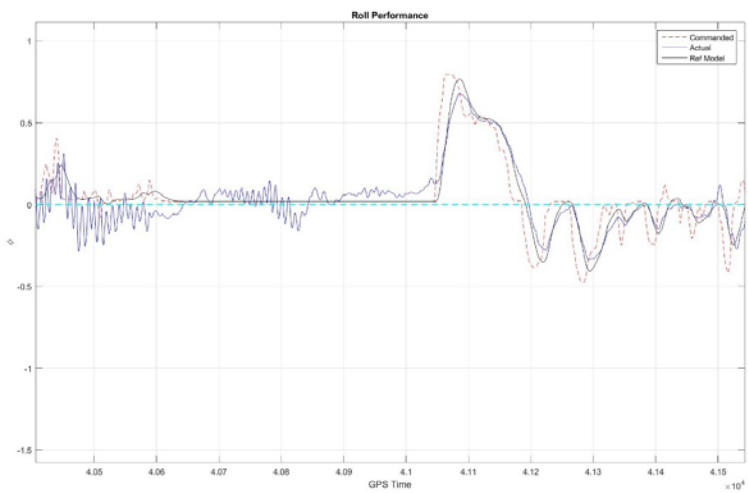

Figure 57: Roll Attitude of Vehicle while Stall Recovery Maneuver

3.3.3 Autonomous Landing

The autonomous landing is one of the flight regimes which require very high collaborative maneuvers, control and planning. We have demonstrated the controller capability in autonomous landing in mathematical simulation environment (MATLAB) and software in loop simulation (XPlane + MATLAB). The adaptive controller is designed to achieve the autonomous landing in presence of cross wind ground effect.

The **cross wind** causes the aircraft to drift aside leading to heading angle misalignment with the runway or even cause sideward drift to miss the runway altogether (Figure 58). The **ground**

effect causes increased lift force and decreased aerodynamic drag (Figure 59). When landing, ground effect can give the pilot the feeling as aircraft is "floating" and can cause bumpy touch down.

Landing basically involves three phases:

- Cruise (Constant Altitude Phase
- Descent Phase
- Flare
    - The flare follows the final approach phase and precedes the touchdown and roll-out phases of landing. In the flare, the nose of the plane is raised, slowing the descent rate, and the proper attitude is set for touchdown.
    - At start of flare the throttle is set to minimum.

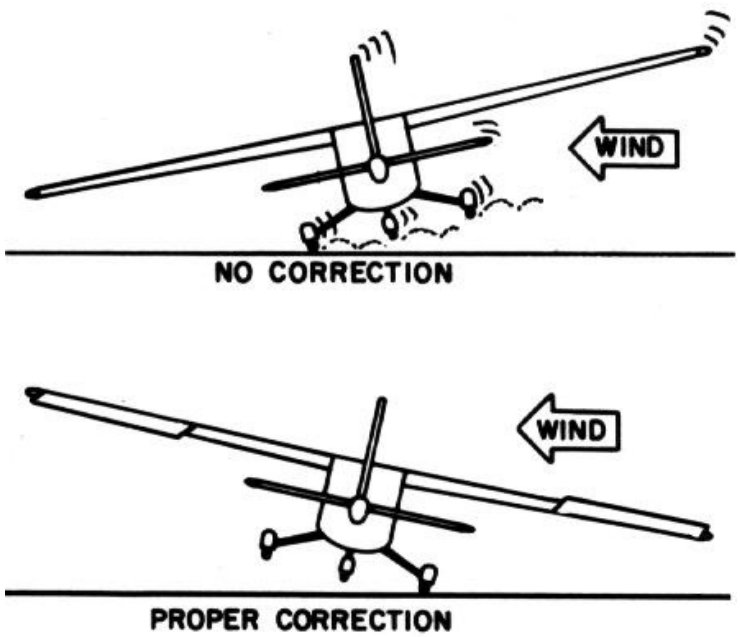

Figure 58: Cross Wind effects on the Landing of Aircraft

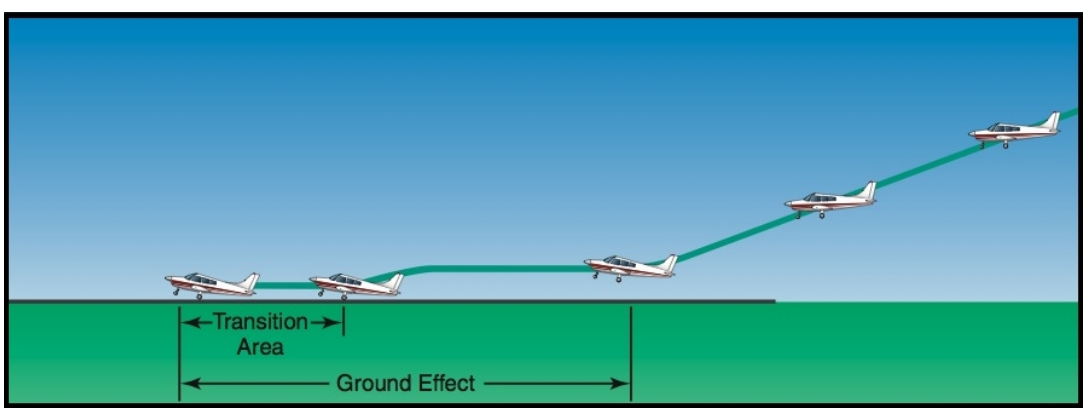

Figure 59: Ground Effect on Landing of Aircraft

The adaptive control accounts for the cross wind effect and ground effect and mitigates their effects on landing maneuver, by online identifying the disturbance and cancelling them. Over all control architecture in pitch and altitude control is shown in Figure 60.

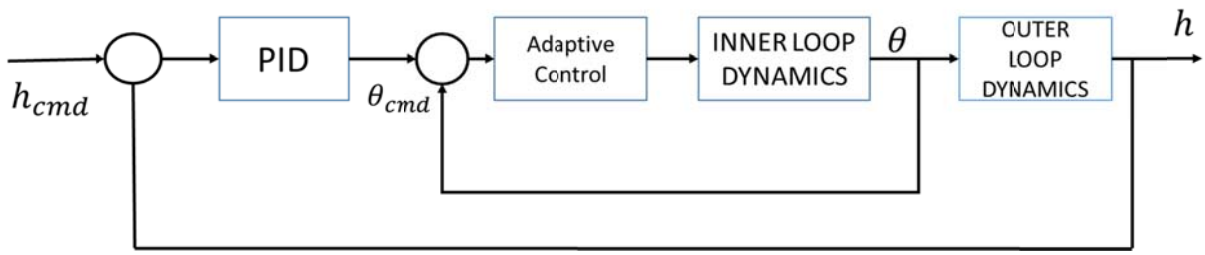

Figure 60: Pitch and Altitude Control to achieve Autonomous Landing

Figure 61 and Figure 62 are MATLAB simulations for autonomous landing. Figure 63 and Figure 64 are plots for landing trajectory and demonstrate the aircraft maneuver to align to runway prior to landing. Figure 65 shows cross track vs altitude and body frame velocity and attitude angles of the UAV while executing autonomous landing. For software simulations no effect of cross wind and ground effect were simulated. Figure 66, Figure 67, and Figure 68 show the SIL results for landing. The cross wind of 10knots is simulated. Since ground effect is very involved aerodynamic interaction experienced by aircrafts, it is uncertain if Xplane simulates such a complicated aerodynamic interaction, hence only way to evaluate autopilot performance in landing with ground effect is by actual flight tests, which will be carried out.

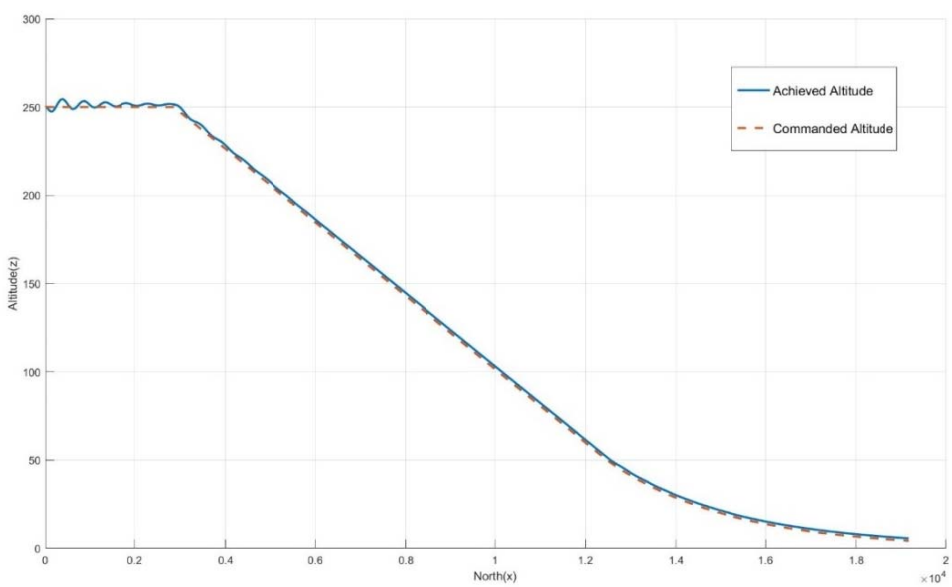

Figure 61: Landing Trajectory: Ground Track vs Altitude

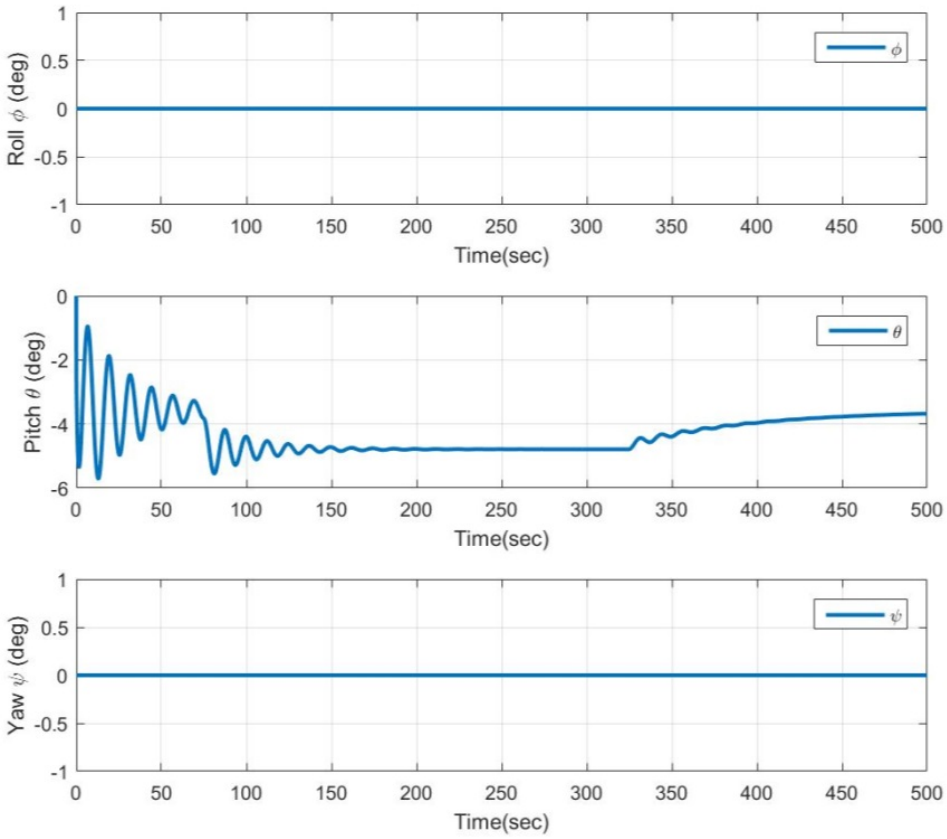

Figure 62: UAV Achieved Attitude Angles Time Plot while Performing Landing

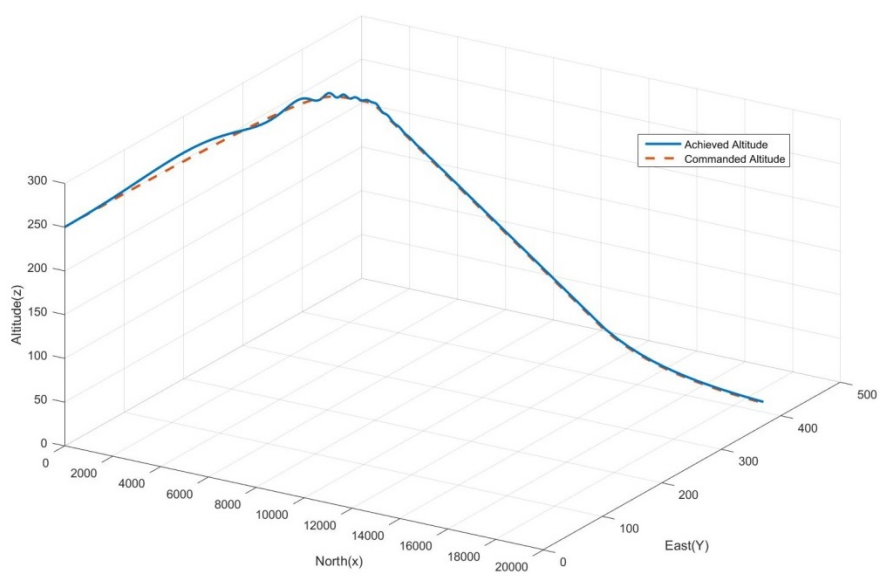

Figure 63: Landing Trajectory: Initial Condition: Course Angle 80 degrees to North, Landing Orientation: 0deg North

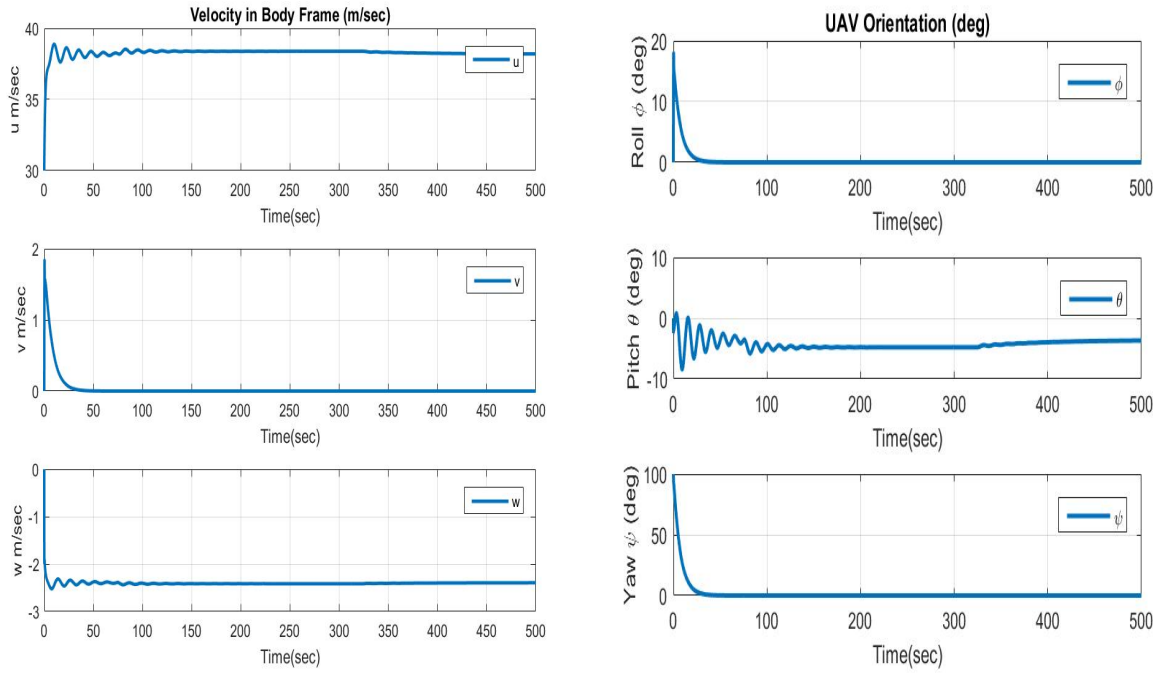

Figure 64: Aircraft Velocities and Attitude Angles in Body Frame, While Executing the Autonomous Landing

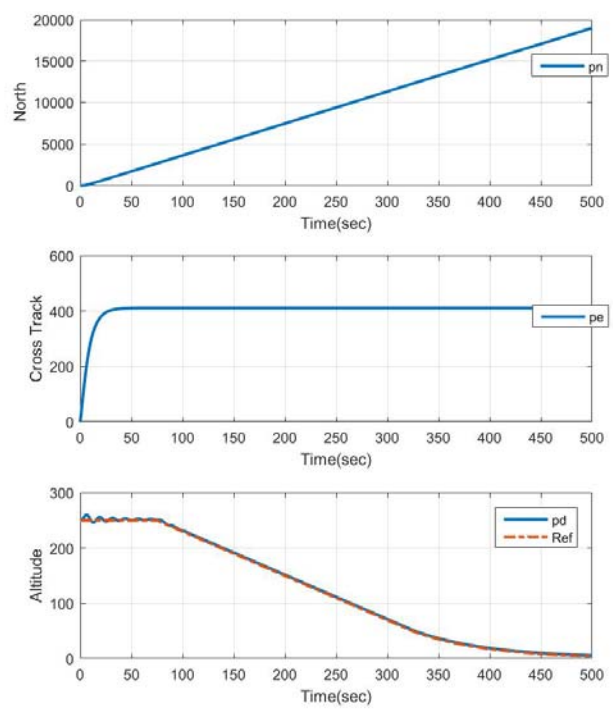

Figure 65: Aircraft Time Plot for Position in Landing Approach and Landing Phase

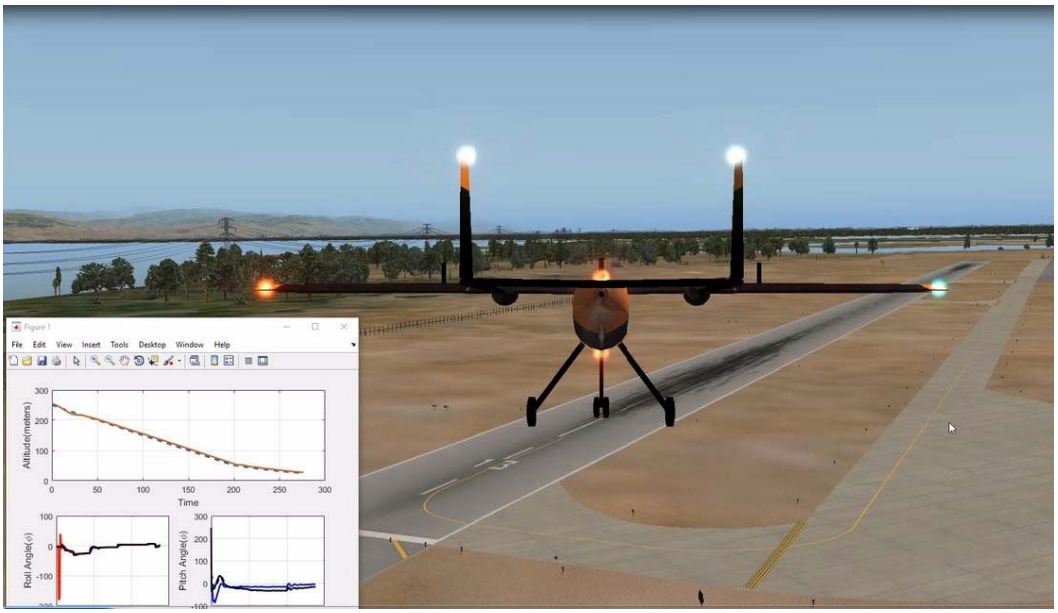

Figure 66: Autonomous Landing in SIL Simulations in Xplane and MATLAB

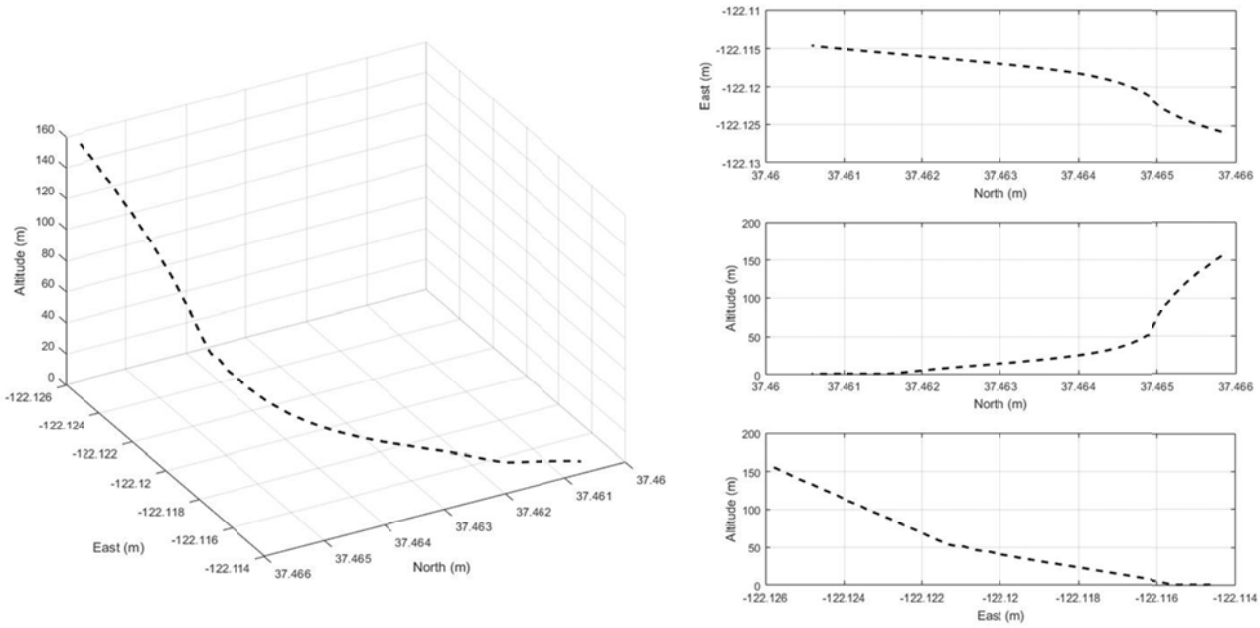

Figure 67: SIL Landing Results: UAV Landing Trajectory, Cross Track (North and East) and Altitude Time Plot

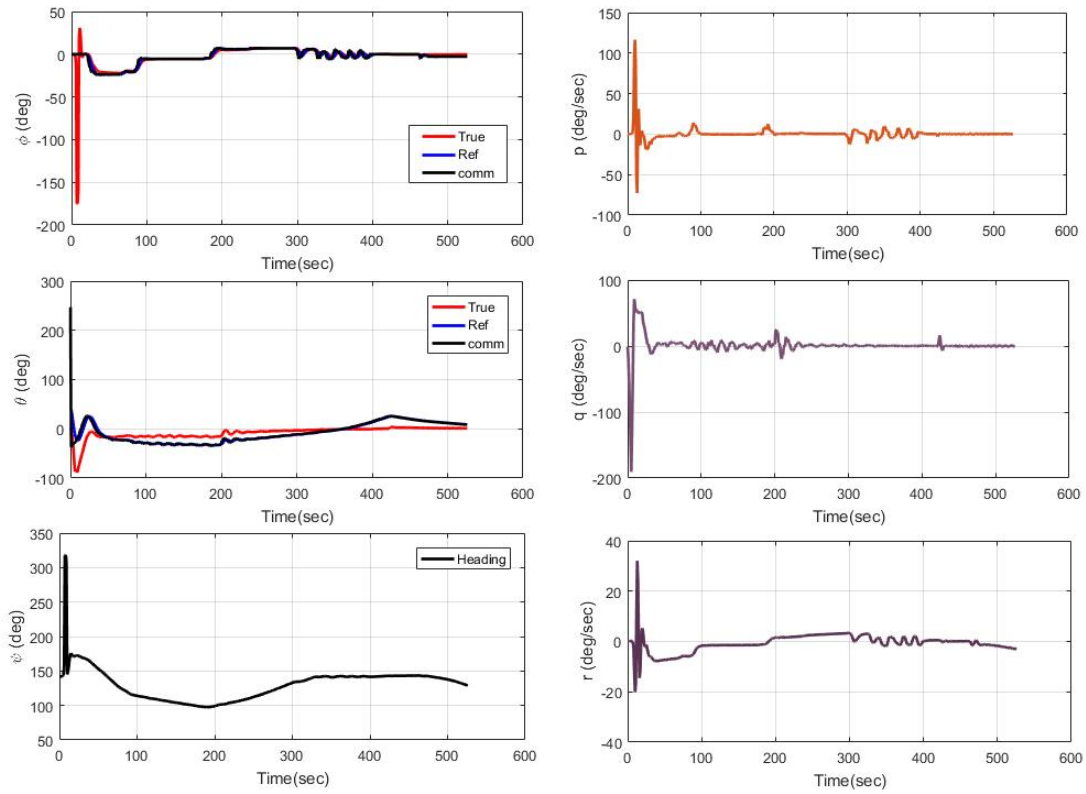

Figure 68: SIL Landing Simulations: UAV Attitude Angle and Body Rates Plots

4 CONCLUSIONS AND RECOMMENDATIONS

In summary, significant progress has been made on several fronts during this LEARN2 program. Key challenges recognized in the proposal have been addressed. The solution framework is identified and implemented.

The newly selected engine provides higher fuel efficiency. The structural weight optimization has led to greater predicted aircraft endurance. It is expected that by more than doubling the fuel capacity will lead to more than 6 hours flight endurance. This flight duration should allow for ample time to complete most payload flight test objectives or complete multiple tests in a single flight.

The study aimed to reduce the weight of the structural wing-box of BASSET unmanned aerial vehicles by optimization. First the original BASSET wing configurations was studied. A NASTRAN FEM was developed based on the CAD model. Then, adjusted pressure distribution for the FEM was developed based on the CFD results for the original BASSET configurations. Subsequent optimization studies showed that 55% of the wing-box weight could be saved by optimized structure. Even for $5\ g$ load case, almost 45% weight reduction is achieved compared to the original design.

A similar optimization study performed for the VEARAT configurations predicted corresponding wing-box weight reduction for the optimized design. However, inclusion of a load case which applied the tail loads during dive into the optimization led to a small increment in the

structural weight owing to the thickening of the spar web and the spar caps at the intersection of the tail boom and the wing.

Autopilot development and integration has resulted in a custom developed GNC system with COTS hardware and open source development software. The GNC system is capable of operating the aircraft through the full flight regime. Additionally the GNC system has ample power and system inputs to allow third party equipment/software to integrate easily within the basset control system.

Overall, the optimization of the baseline BASSET vehicle and the integration of an improved robust control system have created an aircraft uniquely suited to testing and validation of, sensor, payloads, actuators, etc. The large internal volume, extensive power capacity, and 6hr flight endurance would serve as a simply integrated testbed for aircraft, payload, and software developers.

Future structural optimization studies recommended for this project would be investigation of the wing-box structural response in presence of gust loads, and optimal mass placement in presence of strong gusts. HIL testing of sensors, actuators and communication systems and SIL testing of GNC software for safely integrating third party software and hardware shall be part of the future development.

5 REFERENCES

1. "Autonomy Research for Civil Aviation: Toward a New Era of Flight," NRC Report (2014)

NOMENCLATURE

AOA	angle of attack
BASSET	Big Antenna Small Structure Enhanced Tactical
BLOS	Beyond line of sight
CFD	computational fluid dynamics
COTS	commercial off the shelf
CQUAD4	4-noded quadrilateral
CTRIA3	3-noded triangular elements
FEA	Finite Element Analysis
FEM	Finite Element Model
FTS	Flight termination system
GNC	guidance, navigation, and control
HIL	Hardware-in-Loop
INS	Inertial Navigation Systems
KEAS	knots equivalent air speed
L/D	lift/drag
MATLAB	mathematical simulation environment
OML	outer mold line
PSHELL	two-dimensional plate elements
QGC	QGROUNDCONTROL
SIB	Systems Integration Board
SIL	Software-in-Loop
UAV	Unmanned Aerial Vehicle
VEARAT	Versatile Experimental Autonomy Research Aircraft Technology